Near-ground effects of wind turbines: Observations and physical mechanisms

Near-Ground Effects of Wind Turbines: Observations and Physical Mechanisms

SICHENG WU[a] AND CRISTINA L. ARCHER[a]

[a] *Center for Research in Wind, University of Delaware, Newark, Delaware*

(Manuscript received 11 June 2020, in final form 16 December 2020)

ABSTRACT: Wind turbines generate wakes, which can potentially influence the local microclimate near the ground. To verify and quantify such effects, the Vertical Enhanced Mixing (VERTEX) field campaign was conducted in late summer 2016 to measure near-surface turbulent fluxes, wind speed, temperature, and moisture under and outside of the wake of an operational wind turbine in Lewes, Delaware. We found that, in the presence of turbine wakes from a single wind turbine, friction velocity, turbulent kinetic energy, and wind speed were reduced near the ground under the wake, while turbulent heat flux was not significantly affected by the wake. The observed near-ground temperature changes were <0.4°C in magnitude. Near-ground temperature changes due to the wake correlated well with the temperature lapse rate between hub height and the ground, with warming observed during stable and neutral conditions and cooling during unstable conditions. Of the two properties that define a wake (i.e., wind speed deficit and turbulence), the wind speed deficit dominates the surface response, while the wake turbulence remains aloft and hardly ever reaches the ground. We propose that the mechanism that drives changes in near-ground temperature in the presence of turbine wakes is the vertical convergence of turbulent heat flux below hub height. Above hub height, turbulence and turbulent heat flux are enhanced; near the ground, turbulence is reduced and turbulent heat flux is unchanged. These conditions cause an increase (during stable/neutral stability) or decrease (during unstable stability) in heat flux convergence, ultimately resulting in warming or cooling near the ground, respectively.

KEYWORDS: Atmosphere; Boundary layer; Stability; Turbulence; Wind shear; Energy budget/balance

1. Introduction

Wind turbines extract energy from the wind and generate wakes, which are plume-like volumes of low wind speed that form downstream of a turbine. The upper parts of the wakes are also characterized by high turbulent kinetic energy (TKE) and high turbulent fluxes, which cause enhanced vertical mixing above hub height. Vertical mixing significantly impacts the vertical temperature and moisture distribution around the rotor area. For example, at night under stable conditions with warmer air above the rotor than within the rotor area, a wind turbine wake will bring warm air downward from aloft and warm the rotor area, and vice versa in unstable conditions. Because of the ability of a wind turbine wake to redistribute temperature and moisture by vertical mixing in the rotor area, wind farms may have the potential of causing unwanted impacts in the lower atmospheric boundary layer (ABL), such as cooling, warming, drying, etc. The primary goal of this research is to assess the impacts of wind turbine wakes on temperature and humidity in the lower ABL, based on observations, and to propose a mechanism to explain the observed changes.

This is not the first observational study of wind turbine wake effects. Past observational studies either used ground-based instrumentation (Baidya Roy and Traiteur 2010; Rajewski et al. 2016; Smith et al. 2013; Armstrong et al. 2016; Moravec et al. 2018), remote sensing data (Zhou et al. 2012, 2013; Xia et al. 2016; Harris et al. 2014), or wind tunnel measurements (Zhang et al. 2013). Most of them reported near-ground warming at night, except for Moravec et al. (2018), who found no clear long-term effect at wind farms in mountainous regions. For the daytime, however, the effects are still unclear (Zhou et al. 2012, 2013; Rajewski et al. 2014), possibly because the surface boundary layer during the day is generally very turbulent and unstable and therefore the effects of the additional turbulence introduced by the turbines are likely negligible. Neutral conditions have not been well studied in the literature and the associated temperature changes have been generally unclear or nonsignificant (Rajewski et al. 2013). All the studies that found warming at night have attributed the warming to enhanced vertical mixing, implicitly assuming that the enhanced vertical fluxes found in the upper wake region extend all the way down to the ground. Only the Crop Wind Energy Experiment (CWEX) field campaigns (Rajewski et al. 2013, 2014, 2016), however, have provided some evidence of the enhanced vertical mixing by direct measurements of TKE and heat flux near the ground.

Given the cost of performing observational campaigns, many studies of microclimate change by wind farms were conducted using modeling. Wind turbines have been parameterized as increased surface roughness in global climate models (Keith et al. 2004; Barrie and Kirk-Davidoff 2010; Wang and Prinn 2010), as elevated energy sinks and turbulence sources in climate and mesoscale models (Baidya Roy et al. 2004; Jacobson and Archer 2012; Fitch et al. 2012; Volker et al. 2015; Miller and Keith 2018; Sun et al. 2018; Pryor et al. 2019), or as actuator lines/disks in high-resolution large-eddy simulations (LESs) (Lu and Porté-Agel 2011; Calaf et al. 2011; Xie and Archer 2015, 2017; Ghaisas et al. 2017). Most climate modeling studies found a similar nighttime warming pattern as the observational studies (Baidya Roy and Traiteur 2010; Rajewski et al. 2016; Armstrong et al. 2016), with an unrealistically large

Corresponding author: Cristina L. Archer, carcher@udel.edu

DOI: 10.1175/MWR-D-20-0186.1

effect if the simple surface roughness parameterization was used (Fitch 2015). Pryor et al. (2018) reported a small but significant microclimate impact, but confined to the wind farm region and only in summer. In LES studies, however, a reduction of surface vertical mixing, instead of an enhancement, was found (Lu and Porté-Agel 2011; Calaf et al. 2010, 2011; Xie and Archer 2015). A notable numerical study by Xia et al. (2019) stated that the wind speed deficit and the added TKE caused by the turbines have two opposite effects on surface temperature at night. The wind speed deficit causes a reduction of vertical wind shear near the ground, which reduces TKE and produces "a less favorable background environment for turbulent heat fluxes to transport warmer air from aloft to the surface," thus causing cooling. The added TKE increases the magnitude of the downward turbulent heat flux, thus causing warming near the surface. We note a few limitations of the study by Xia et al. (2019), including the use of an idealized wind turbine model, the use of the Fitch parameterization (Fitch et al. 2012) at the finest recommended resolution (1 km) (Fitch 2016), and the recently identified bug in the WRF Model with the Fitch parameterization (Archer et al. 2020).

From the literature it appears that the effects of wind turbine wakes on near-ground properties are complex to understand, measure, simulate, and predict. Not surprisingly, there are many inconsistencies between the observed effects and the supposed mechanism, i.e., enhanced vertical mixing. For example, warming was observed also during cloud-free days in the remote sensing study by Zhou et al. (2012), when cooling would be expected if vertical mixing was enhanced near the ground. A reduction of vertical mixing near the ground was reported in all LES studies, which would cause cooling, not warming, during stable conditions. In the CWEX campaigns (Rajewski et al. 2013, 2014, 2016), numerous findings were not consistent with vertical mixing near the ground and the observed atmospheric stability.

To try to clarify these inconsistencies, the Vertical Enhanced Mixing (VERTEX) field campaign was conducted in Lewes, Delaware, near a Gamesa G90–2MW wind turbine, from late August to early October 2016, to measure the turbulent fluxes, wind speed, and temperature near the ground. Archer et al. (2019) already discussed the VERTEX setup and some preliminary findings on the lack of enhanced vertical mixing near the ground in the presence of a wind turbine wake, thus only a brief description of VERTEX is provided in section 2. The methods to identify and analyze the wake events are described in section 3. The findings on the effects of wind turbine wakes on surface microclimate properties (e.g., temperature) and vertical mixing properties (e.g., friction velocity u_*) are reported in section 4. Last, the proposed mechanism to explain the changes in near-surface temperature caused by wind turbine wakes is described in section 5.

2. Description of the VERTEX field campaign

The VERTEX field campaign was conducted in Lewes, Delaware, in August–October 2016. A total of 15 flux towers, equipped with sonic anemometers and temperature/humidity sensors were deployed in the Great Marsh to the southwest of a Gamesa G90–2MW wind turbine, with a hub height (H) of 78 m and a rotor diameter (D) of 90 m (Fig. 1). Of these 15 flux towers, 3 were placed at a distance of 5D from the turbine (close-wake), 3 were 5–10D (midwake), and the other 9 were farther than 10D (distant-wake). For the same radial distance from the turbine, the flux towers were spaced laterally so that the wake would only affect one of them. Details about the instruments installed on each surface station can be found in Table 1. Tilt correction and quality control were applied for the measurements of the sonic anemometers (Archer et al. 2019).

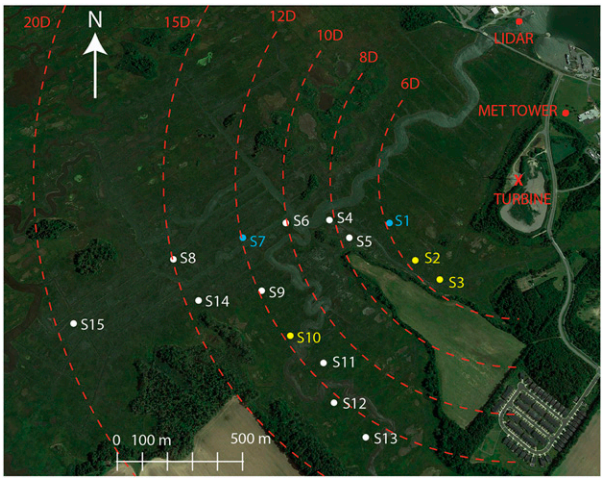

FIG. 1. Layout of the VERTEX field campaign. S1–S15 are the locations of the surface flux stations. The sites in blue are reference stations (or "no-wake") and those in yellow are the wake stations analyzed in detail in the rest of the paper.

At a distance of approximately 4D northeast (upwind) of the wind turbine was a meteorological tower (called "met tower" hereafter), which measured wind speed, temperature, and humidity at 10, 25, 33, 42, and 49 m. For each height, two 2.5-m booms were set up in the southeast and northwest directions.

A lidar was installed at the site to the north of the wind turbine (Fig. 1). The lidar was configured to scan in plan position indicator (PPI) mode, with fixed elevation angles from 2.6° to 15.8° listed in Table 1 with a sampling time of 2 min each, and azimuth angles from 174° to 270°, which covered the whole VERTEX field. The scanning patterns are described in Archer et al. (2019) with more detail.

3. Methods

a. Vertical mixing variables and atmospheric stability

The variables that will be used in this study to characterize vertical mixing are friction velocity (u_*), virtual heat flux ($\overline{w'T_v'}$), TKE, and $\overline{w'w'}$. The first three variables are commonly used in the literature (Lu and Porté-Agel 2011; Rajewski et al. 2013, 2014); the last variable, the vertical flux of vertical momentum, will be justified below.

The vertical transport of turbulent momentum can be described by the nondiagonal terms of the Reynolds stress tensor that are associated with the vertical direction, $\overline{u'w'}$ and $\overline{v'w'}$, which are part of friction velocity as follows:

TABLE 1. Details of the instrumentation used for VERTEX. The elevation angles of the lidars used for the wake detection are in boldface. Reproduced with permission from Archer et al. (2019, their Table 1).

Sensor type	Sensor model	Accuracy	Location(s)	Height above ground or resolution (m) or lidar elevation angle (°)
3D sonic anemometer	Campbell CSAT3	$<\pm0.08\,\mathrm{m\,s^{-1}}$	S1–S15	3
2D sonic anemometer	Gill Wind Observer	±2%	S1–S15	10
T–RH probe	NCAR SHT75	T: ±0.3°C; RH: ±1.8%	S1–S15	3
Air pressure	Vaisala PTB220	±0.15 hPa	S1, S3, S15	2
Soil moisture	Decagon EC-5	±2%	S1, S9, S15	−0.05
Soil heat flux	REBS	±5%	S1, S9, S15	−0.05
Soil temperature	NCAR	–	S1, S9, S15	−0.01, −0.05
Infrared gas analyzer	Campbell EC-150	CO_2: ±1%; HO_2: ±2%	S13, S15	3
3D sonic anemometer	RMYoung 81000	$\pm0.05\,\mathrm{m\,s^{-1}}$	MetT	10, 25, 33, 42, 49
T–RH probe	RMYoung 41382LC	T: ±0.3°C; RH: ±1%	MetT	10, 25, 33, 42, 49
Scanning lidar	Windcube 200S	$<\pm0.5\,\mathrm{m\,s^{-1}}$	L1	PPI: **2.6, 4.1, 5.6,** 6.1, 7.1, 8.6, 10.1, 11.6, 13, 14.4, 15.8

$$u_*^2 = \sqrt[2]{\overline{u'w'}^2 + \overline{v'w'}^2}. \tag{1}$$

The vertical transport of heat in VERTEX is described by $\overline{w'T'_v}$, which is the correlation of vertical velocity and virtual temperature. As discussed in Archer et al. (2016) and Rajewski et al. (2016), virtual temperature T_v can be approximated by the sonic temperature from the sonic anemometers T_s. A positive (upward) $\overline{w'T'_v}$ is generally associated with unstable conditions, while a negative (downward) $\overline{w'T'_v}$ is generally associated with stable conditions.

TKE is calculated from the turbulent normal stresses (i.e., the diagonal terms in the Reynolds stress tensor) as follows:

$$\mathrm{TKE} = \frac{1}{2}\left(\overline{u'u'} + \overline{v'v'} + \overline{w'w'}\right). \tag{2}$$

Note that the third term in parenthesis in Eq. (2) is the vertical flux of vertical momentum $\overline{w'w'}$, which is the only term out of three that accounts for fluctuations of wind in the vertical. Thus, TKE is not adequate in studies, like this one, in which the focus is on vertical, not horizontal, mixing, because horizontal fluctuations dominate TKE (as also demonstrated later in Figs. 4–6). However, since it is widely used as a proxy for mixing, TKE will be discussed in this study too.

The turbulent linear correlation coefficients are used as a measure of the efficiency of turbulent transfer (Roth and Oke 1995; Rajewski et al. 2014). For momentum transfer:

$$r_{u_*} = \frac{u_*^2}{\sigma_w\sqrt{\sigma_u^2 + \sigma_v^2}} \tag{3}$$

and for heat transfer:

$$r_{wT_v} = \frac{\overline{w'T'_v}}{\sigma_w\sigma_{T_v}}, \tag{4}$$

where σ_u, σ_v, and σ_w are the standard deviations of the u, v, and w components of the wind vector, and σ_{T_v} is the standard deviation of virtual temperature. The Reynolds averaging time needed to calculate turbulent covariances should be long enough to cover all significant flux-carrying wavelengths, especially for vertical momentum flux, but short enough to capture important nonstationary events, like wakes. Ogive analysis is often used to identify the proper averaging time (Oncley et al. 1996; Sievers et al. 2015). Ogive is the cumulative integration of spectral density over a range of frequencies:

$$\mathrm{Og}_{xy} = \int_{\infty}^{f_0} \mathrm{Co}_{xy}(f)\,df, \tag{5}$$

where x and y are two variables of interest, e.g., wind speed components (u, v, and w) or sonic temperature T_v; and Co_{xy} is the cospectrum of x and y. The inverse of the lowest frequency at which Og_{xy} converges is the desired averaging time.

Examples of 2-h Ogives Og_{uw} and Og_{wT_v} at station S3 are shown in Fig. 2. Between 0800 EST 4 September and 0400 EST 5 September, a variety of stability and wind speed conditions were observed, which is reflected in the ogives in two ways. First, the ogives values varied by at least an order of magnitude and, second, the ogives converged at different frequencies at different hours. However, for frequencies lower than 1.1×10^{-3} Hz (blue line in Fig. 2), corresponding to an averaging time of 15 min, all the ogives became flat and therefore convergence was achieved. The same general behavior was also observed on other days/times (not shown). As such, the statistics in this study are calculated over a 15-min averaging period. Additional details about the averaging and postprocessing of the VERTEX data can be found in section 3.1 of Archer et al. (2019).

It is known that, to understand stability in the lower boundary layer, a local observation near the ground may not be sufficient (Schotanus et al. 1983; Stull 1988). The temperature lapse rate calculated using the virtual temperature measured by the sonic anemometer between 49 and 10 m at the met tower, hereafter referred to as the ''lower-rotor lapse rate'' Γ_{LR}, was used for atmospheric stability in VERTEX:

$$\Gamma_{\mathrm{LR}} = -\frac{\Delta T_v}{\Delta z} = -\frac{T_{v,49} - T_{v,10}}{49\,\mathrm{m} - 10\,\mathrm{m}}. \tag{6}$$

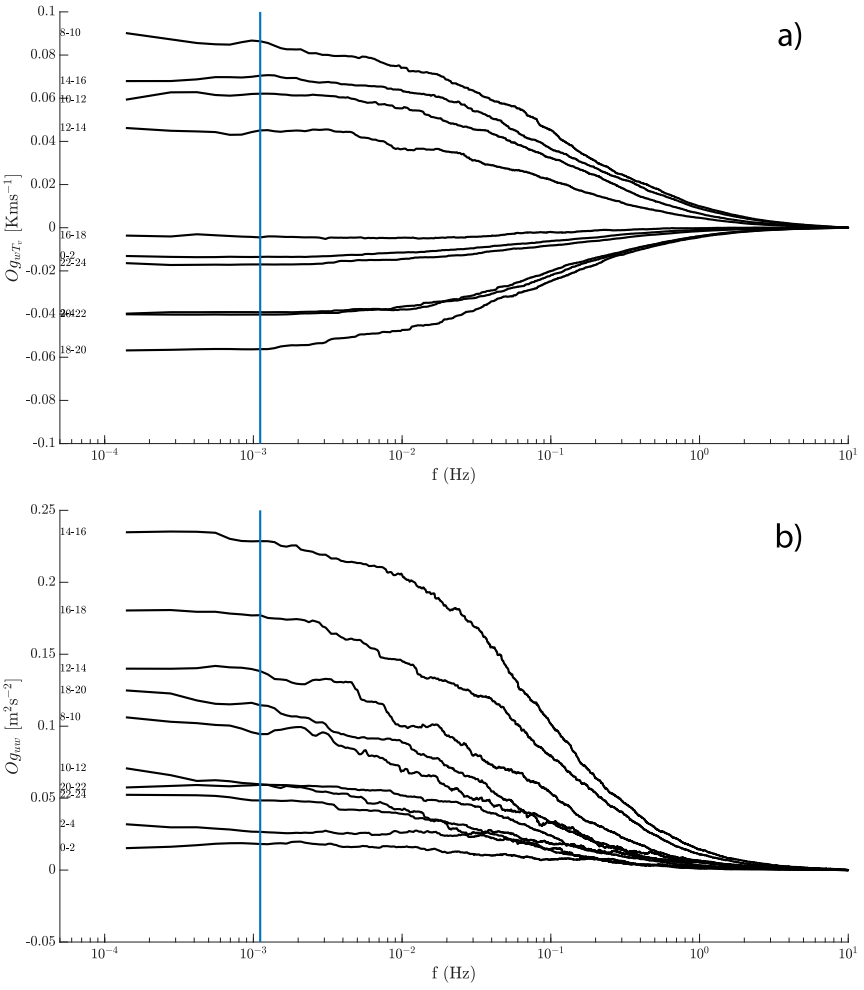

FIG. 2. Ogives from 2-h cospectra of (a) u and w and (b) w and T_v between 0800 EST 4 Sep and 0400 EST 5 Sep 2016. The vertical line corresponds to the 15-min averaging period. The labels on the left of the curves are the 2-h time periods included in each line.

Stability was determined by comparing Γ_{LR} against the dry adiabatic lapse rate ($\Gamma_d = 0.0098\,\mathrm{K\,m^{-1}}$) using an uncertainty margin of $\pm 0.002\,\mathrm{K\,m^{-1}}$ as follows:

- Stable: $\Gamma_{LR} \leq 0.008\,\mathrm{K\,m^{-1}}$
- Neutral: $0.008 < \Gamma_{LR} \leq 0.012\,\mathrm{K\,m^{-1}}$
- Unstable: $\Gamma_{LR} > 0.012\,\mathrm{K\,m^{-1}}$

b. *Identification of wake events*

Since the line-of-sight of lidar L1 was not always aligned with the wind directions that cause wakes over the marsh (Bodini et al. 2017), only wake events with a prevailing wind direction from the north-northeast at 49 m could be identified with certainty. Note that Archer et al. (2019) did not adopt such a stringent criterion. Because of these limitations, only wake events for which sites S2 and S3 in the close-wake region and site S10 in the distant-wake region were under the wake are considered here. When site S1 was under the wake, for example, the wind direction was too easterly and therefore too far off from the line-of-sight of the lidar L1 (Fig. 1). Also, only cases when the wind turbine generated more than 100 kW of power, or the wind speed at the met tower (at 49 m) was greater than $5\,\mathrm{m\,s^{-1}}$, were considered. The PPI lidar scans at the three lowest elevation angles (2.6°, 4.1°, 5.6°) were analyzed because at these elevation angles the wind turbine wakes could be intercepted by the laser beam. For these PPI scans, a −28 dB Carrier-to-Noise Ratio (CNR) threshold was applied to remove unrealistic radial velocities (Bodini et al. 2017). Then the location of the wake was determined by the wake detection algorithm of Wang and Barthelmie (2015). With this algorithm, it was possible to clearly identify which surface flux stations were under the wake and which were not, as discussed in Archer et al. (2019).

When a wake was observed over the VERTEX area via the wake detection algorithm and all the above requirements were met, the wake could last between half an hour (i.e., the average interval between two successive lidar scans at the same elevation angle) and several hours; it could sweep or meander

over several surface flux stations; and it could possibly even come back and forth over a given station multiple times.

Seventeen wake events were identified during the 3-month long VERTEX campaign. The largest majority of wake events occurred under stable and neutral conditions. In the Results section, three representative wake events will be examined with lidar scans and time series of observed mixing properties at the site under the wake (wake station) and at a control site that was not under the wake (no-wake station).

c. *Difference-in-differences*

When a site was under the wake, the wind direction at the 49-m level of the met tower was not constant but rather varied within a certain range. For the statistical analysis, we defined the wake range as that between the 12.5% and 87.5% quantiles of wind direction. For example, for the close-wake stations, the width of the wake range was between ±6° to ±9° (i.e., 12° to 18°), depending on the site, which is slightly larger than the commonly used ±5° expansion of the wind turbine wake (Barthelmie et al. 2010), but smaller than the 32°–40° ranges used in Rajewski et al. (2014). The wake ranges are not symmetrical around the direction of alignment between the turbine and the site, possibly due to wind veering, wake meandering, wake swinging, or yaw misalignment.

We then used the 49-m wake range as the proxy to discriminate whether a measurement at a given site occurred under the wake or not. Here we focus on three ''wake stations'', two in the close-wake region (S2 and S3) and one in the distant-wake region (S10), each paired with a ''reference'' site (S1 for the close-wake and S7 for the distant-wake), also called ''no-wake station.'' Following Rajewski et al. (2014), we calculated the differences in mixing properties and other meteorological variables at the three pairs of station (S2–S1, S3–S1, and S10–S7) during both wake and no-wake conditions. The no-wake conditions are those when neither station in the pair was under the wake (i.e., with wind from the north, between −15° and +10°). The wake conditions are those when the wake station (S2, S3, or S10) was under the wake but the no-wake station (S1 or S7) was not.

This approach of comparing differences between a station pair during wake and no-wake conditions, called Difference-in-Difference (DiD), is necessary to properly account for potential systematic biases, like spatial inhomegeneities, that may affect one site of the pair but not the other and would therefore interfere with the wake signal. For example, if site A was clear of any obstacles but site B was located behind a tall bush patch, site B would experience blockage from the bush patch and therefore lower wind speed than site A. Let us say that the wake hits site B and causes a further wind speed reduction. If we just compare site B versus A, we would see a very strong wind speed reduction at B relative to A, which we would entirely attribute to the wake. However, if the wake hits site A, the two sites may end up having the same wind speed and we would therefore reach the contradictory conclusion that the wake did not have an effect on site A. But if we take the difference in wind speed between site A and B, we would know that it is positive in the absence of a wake due to the bush patch at B and we would be able to subtract this initial positive

TABLE 2. Differences in observed mixing properties between the wake station and the reference station (suffix ''0'') during each of the nine wake events and during their reference periods (''Ref''). The standard deviation of each difference is indicated in parentheses. Values are in boldface when the changes are significant and negative (i.e., decreases) and in boldface and italic when the changes are significant and positive (i.e., increases).

Wake event ID	Reference station	Wake station	Reference period (EST)	Wake period (EST)	$\frac{\Delta u_*}{u_{*0}}$		$\frac{\Delta\lvert\overline{w'T'_v}\rvert}{\lvert\overline{w'T'_{v0}}\rvert}$		$\frac{\Delta\overline{w'w'}}{\overline{w'w'_0}}$		$\frac{\Delta\mathrm{TKE}}{\mathrm{TKE}_0}$		$\frac{\Delta U}{U_0}$		ΔT (K)	
					Ref	Wake	Ref	Wake	Ref	Wake	Ref	Wake	Ref	Wake	Ref	Wake
Aug30-S-1	S1	S2	0000–0045	0053–0144	**0.00 (0.03)**	**−0.17 (0.10)**	−0.05 (0.10)	−0.12 (0.21)	−0.07 (0.01)	−0.07 (0.18)	**0.10 (0.08)**	**−0.01 (0.10)**	**−0.27 (0.14)**	**−0.68 (0.16)**	***−0.10 (0.03)***	***0.03 (0.04)***
Aug30-S-2	S1	S3	0230–0300	0430–0545	**−0.10 (0.01)**	**−0.35 (0.07)**	−0.21 (0.06)	−0.29 (0.14)	**−0.22 (0.05)**	**−0.36 (0.11)**	−0.29 (0.20)	−0.29 (0.12)	**−0.31 (0.03)**	**−0.59 (0.16)**	***−0.09 (0.08)***	***0.08 (0.05)***
Sep04-S	S1	S3	1:00–0500	1900–2300	**0.00 (0.06)**	**−0.15 (0.11)**	−0.22 (0.15)	−0.11 (0.09)	**0.43 (0.18)**	**−0.12 (0.18)**	0.18 (0.09)	−0.02 (0.23)	−0.63 (0.15)	−0.69 (0.41)	0.09 (0.04)	0.14 (0.10)
Sep11-S	S1	S3	2300–2330	2330–0025	−0.05 (0.06)	−0.12 (0.13)	0.12 (0.08)	0.05 (0.13)	**0.16 (0.04)**	**−0.11 (0.11)**	0.07 (0.13)	−0.01 (0.14)	−0.91 (0.32)	−0.83 (0.49)	***−0.13 (0.10)***	***0.00 (0.02)***
Sep12-S	S1	S2	2300–2330	0036–0107	**−0.01 (0.02)**	**−0.13 (0.00)**	**0.09 (0.05)**	**−0.16 (0.01)**	−0.04 (0.07)	−0.09 (0.07)	−0.04 (0.00)	−0.02 (0.05)	**−0.15 (0.09)**	**−0.61 (0.18)**	***−0.17 (0.08)***	***0.14 (0.06)***
Sep15-S	S1	S2	0200–0300	0345–0545	−0.1 (0.04)	−0.12 (0.07)	−0.14 (0.04)	−0.07 (0.08)	**−0.08 (0.05)**	**−0.14 (0.04)**	***−0.05 (0.14)***	***0.09 (0.08)***	**−0.27 (0.32)**	**−0.79 (0.23)**	***−0.18 (0.03)***	***0.04 (0.03)***
Sep20-N-1	S1	S3	0100–0130	0130–0200	**−0.11 (0.08)**	**−0.23 (0.01)**	0 (0.13)	1.63 (2.59)	**−0.15 (0.11)**	**−0.28 (0.02)**	−0.01 (0.48)	−0.18 (0.10)	**−0.53 (0.12)**	**−0.77 (0.21)**	−0.01 (0.01)	0 (0.02)
Sep20-N-2	S1	S3	0100–0130	0230–0300	**−0.11 (0.08)**	**−0.25 (0.13)**	**−0.00 (0.13)**	**−0.37 (0.35)**	**−0.15 (0.11)**	**−0.28 (0.08)**	−0.01 (0.48)	−0.29 (0.10)	**−0.53 (0.12)**	**−0.79 (0.06)**	−0.01 (0.01)	−0.06 (0.03)
Sep25-U	S1	S3	1100–1200	0900–1000	**0.03 (0.05)**	**−0.09 (0.07)**	0.01 (0.17)	−0.12 (0.04)	0.05 (0.13)	−0.03 (0.06)	***−0.06 (0.09)***	***0.10 (0.09)***	**−0.02 (0.11)**	**−0.15 (0.04)**	0.01 (0.13)	−0.05 (0.10)

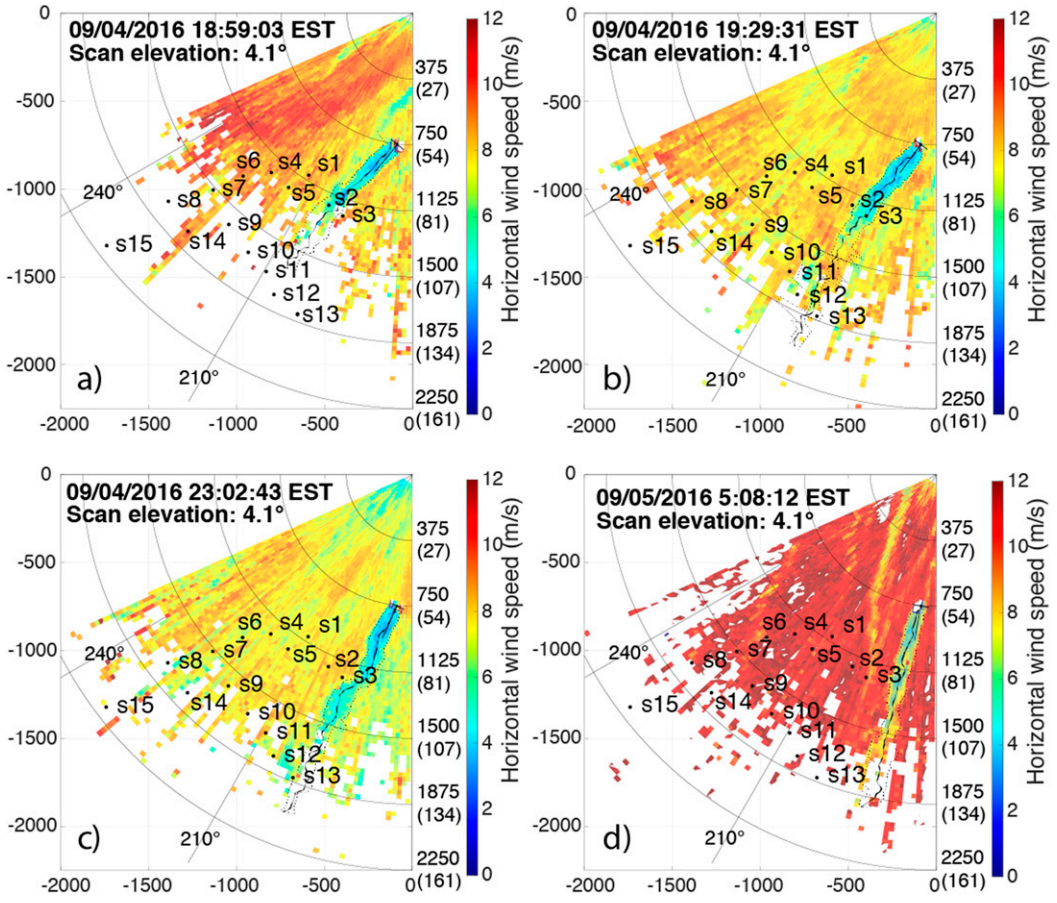

FIG. 3. Horizontal wind speed distribution from lidar L1 during the wake event of 4–5 Sep 2016: (a) just before the wake hits S3, (b) beginning of the wake period when S3 is under the wake, (c) end of the wake period when the wake moved to the east of the field, and (d) end of the reference period. The circles centered at L1 in the upper-right corner show the distances in m (with elevation in parentheses, in m) from L1.

difference from the differences obtained during wake conditions. The true effect of the wake is therefore the net of the two, i.e., the difference during wake conditions minus the difference during no-wake conditions.

4. Results

In section 4a we describe three examples of wake events, during which the lidar's line-of-sight was aligned with the wind direction, the wake lasted enough to impact the wake station but not the no-wake station, and a reference period was identified during which none of the stations in the pair was under the wake. These cases provide valuable information about the wake behavior and near-ground vertical mixing. Details about all wake events can be found in Table 2. In section 4b we describe the results of the statistical analysis applied to the entire VERTEX campaign period, inclusive of both close- and distant-wake stations.

a. Wake event examples

In this section, we quantify the effect of the wake by calculating the difference of six properties—u_*, TKE, $\overline{w'w'}$, U, $\overline{w'T_v'}$, and 2-m temperature—between the wake station and the reference station. With the exception of $\overline{w'T_v'}$ and 2-m temperature, the difference is normalized by the value of the property of interest at the reference station. Values will be reported as the mean plus and minus one standard deviation.

1) STABLE: 4–5 SEPTEMBER

During the wake event of 4–5 September, the sky was clear, relative humidity stayed around 68% and the upwind wind speed at 49 m (measured by met tower) was 7–9 m s^{-1}. Based on the met tower profile, this was a stable case. The location of the wake is shown in the lidar scans in Fig. 3 and the 15-min time series of friction velocity u_*, TKE, $\overline{w'w'}$, and horizontal wind speed U are shown in Fig. 4. The wake moved over S3 at 1900 EST and moved to the east of the field after 2300 EST. Therefore, the wake period was selected from 1900 to 2300 EST and the reference period lasted from 0100 EST, when S3 completely recovered from the wake effect, to 0500 EST. During these two periods the upwind wind speed and temperature were nearly identical.

Starting with friction velocity (Fig. 4a), the magnitude of u_* at the wake station S3 and at the no-wake station S1 was similar

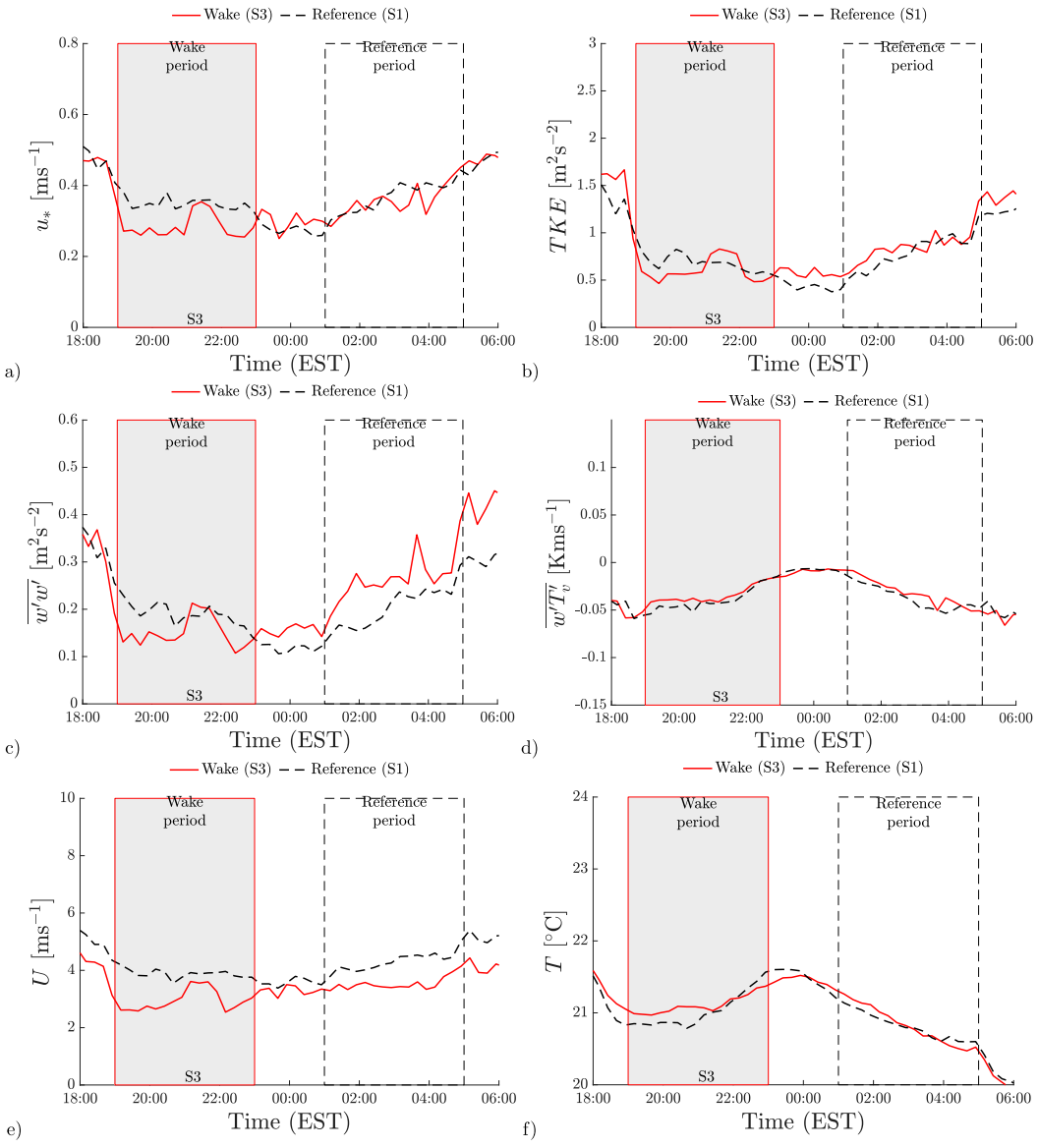

FIG. 4. The 15-min time series during the stable wake event of 4–5 Sep 2016: (a) friction velocity u_*, (b) TKE, (c) $\overline{w'w'}$, (d) turbulent heat flux $\overline{w'T_v'}$, (e) horizontal wind speed U at 3 m, and (f) temperature at 2 m. The wake station is S3 and the no-wake station is S1.

during the reference period (dashed rectangle). During the wake period (gray rectangle), however, u_* at S3 was lower than at S1, with a normalized difference of -0.18 ± 0.09 compared to -0.03 ± 0.09 in the reference period. TKE and $\overline{w'w'}$ (Figs. 4b,c) shared a similar pattern, with the wake station S3 having a higher value than the no-wake station during the reference period (red line on top of black line), but the opposite when the wake hits S3 (red line below the black line). The normalized differences are -0.10 ± 0.18 and -0.20 ± 0.17 for TKE and $\overline{w'w'}$ when S3 is under the wake, while 0.09 ± 0.13 and 0.32 ± 0.20, respectively, when S3 is outside of the wake. This indicates that a reduction of mixing occurred below the wake, although the standard deviations were higher than those of u_*. The wind speed (Fig. 4e) was slightly lower at S3 than at S1 when S3 was outside of the wake, but the difference became even larger when S3 was under the wake. Note that from 2100 to 2200 EST there was a short-lived wind speed burst that caused wind speed to bump up by $1\,\mathrm{m\,s^{-1}}$ at S3 only, which also caused a bump in u_* (Fig. 4a) and TKE (Fig. 4b) during this period, but the reduction of mixing and wind speed still hold.

The turbulent heat fluxes at the two stations were similar throughout the night (Fig. 4d). A slight increase in temperature was observed when S3 was under the wake, compared to the reference period, during which the temperature was nearly the same between the two stations (Fig. 4f).

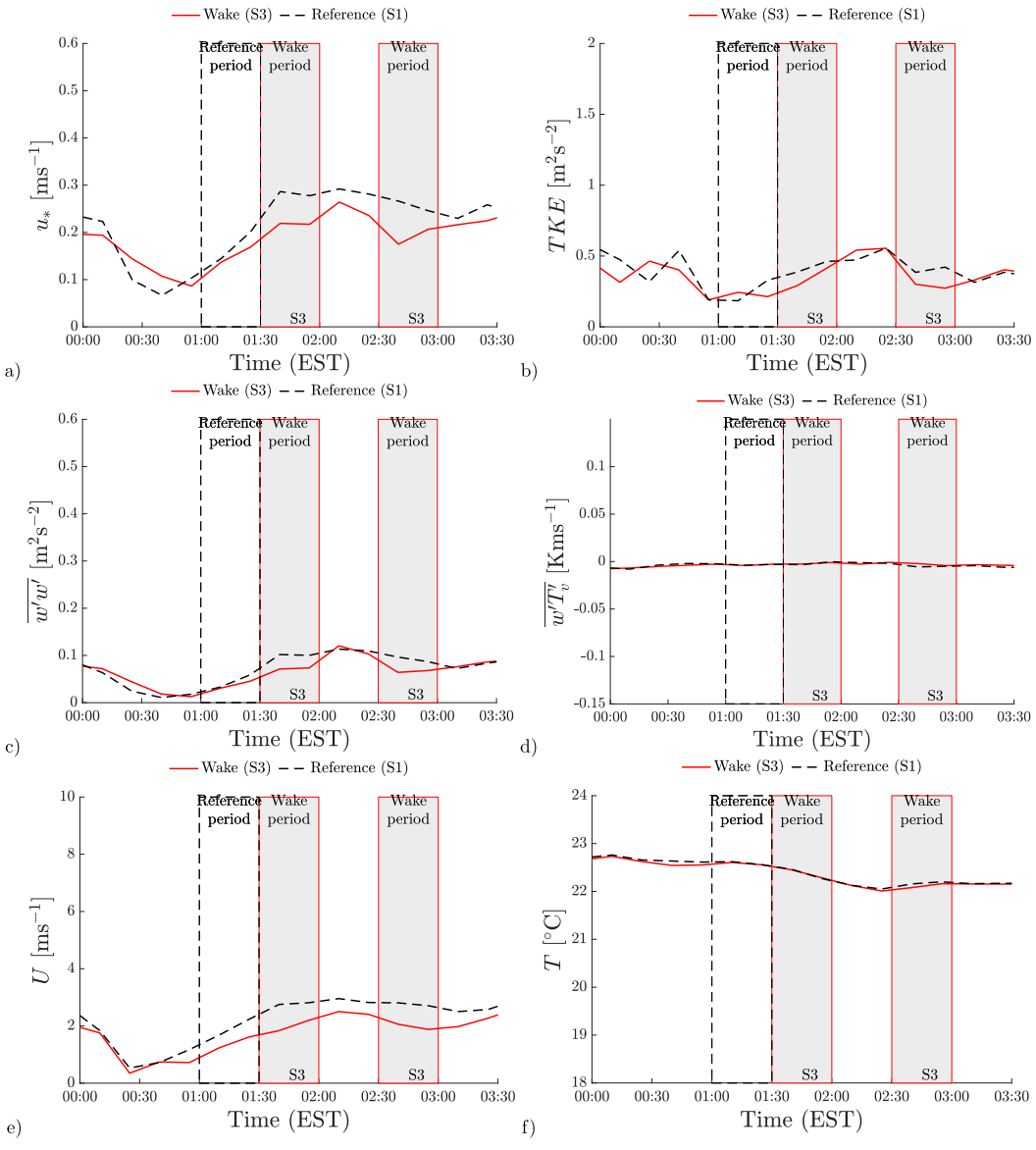

FIG. 5. As in Fig. 4, but for the neutral wake event of 20 Sep 2016.

2) NEUTRAL: 20 SEPTEMBER

The cloudy, high-humidity (>95%) and low-wind speed (4–5 m s^{-1} at 49 m) meteorological conditions of this wake event were already discussed in Archer et al. (2019), including the lidar scans. During the reference period from 0100 to 0130 EST (Fig. 5), neither S1 (no-wake station) nor S3 (wake-station) were under the wake, while S3 was under the wake twice, from 0130 to 0200 EST and from 0230 to 0300 EST. The atmospheric stability during this case was neutral (not shown).

Similar to the wake event of 4 September, a decrease in vertical mixing and horizontal wind speed was observed. A significant reduction of normalized friction velocity was found under the wake for both of the wake periods (gray-shaded areas in Fig. 5a), from -0.11 ± 0.08 in the reference period to -0.23 ± 0.01 and -0.25 ± 0.13, respectively. The normalized wind speed dropped from -0.53 ± 0.12 in the reference period to -0.77 ± 0.21 and -0.79 ± 0.06 under the wake (Fig. 5e). A decrease in TKE and $\overline{w'w'}$ were also observed (Figs. 5b,c), although the standard deviation in TKE during the reference period was large and statistical significance was not achieved. The temperature and heat flux changes caused by the wind turbine wake were negligible (Figs. 5d,f).

3) UNSTABLE: 25 SEPTEMBER

During the daytime on 25 September, relative humidity was moderate (50%–60%), the sky was clear, and no rainfall occurred. The air temperature was nearly constant around 18°C; wind speed stayed at 6–8 m s^{-1} at 49 m. In the morning, the turbine did not turn on until 0830 EST. Then the wake was above S3 from 0830 to 1000 EST and gradually moved to

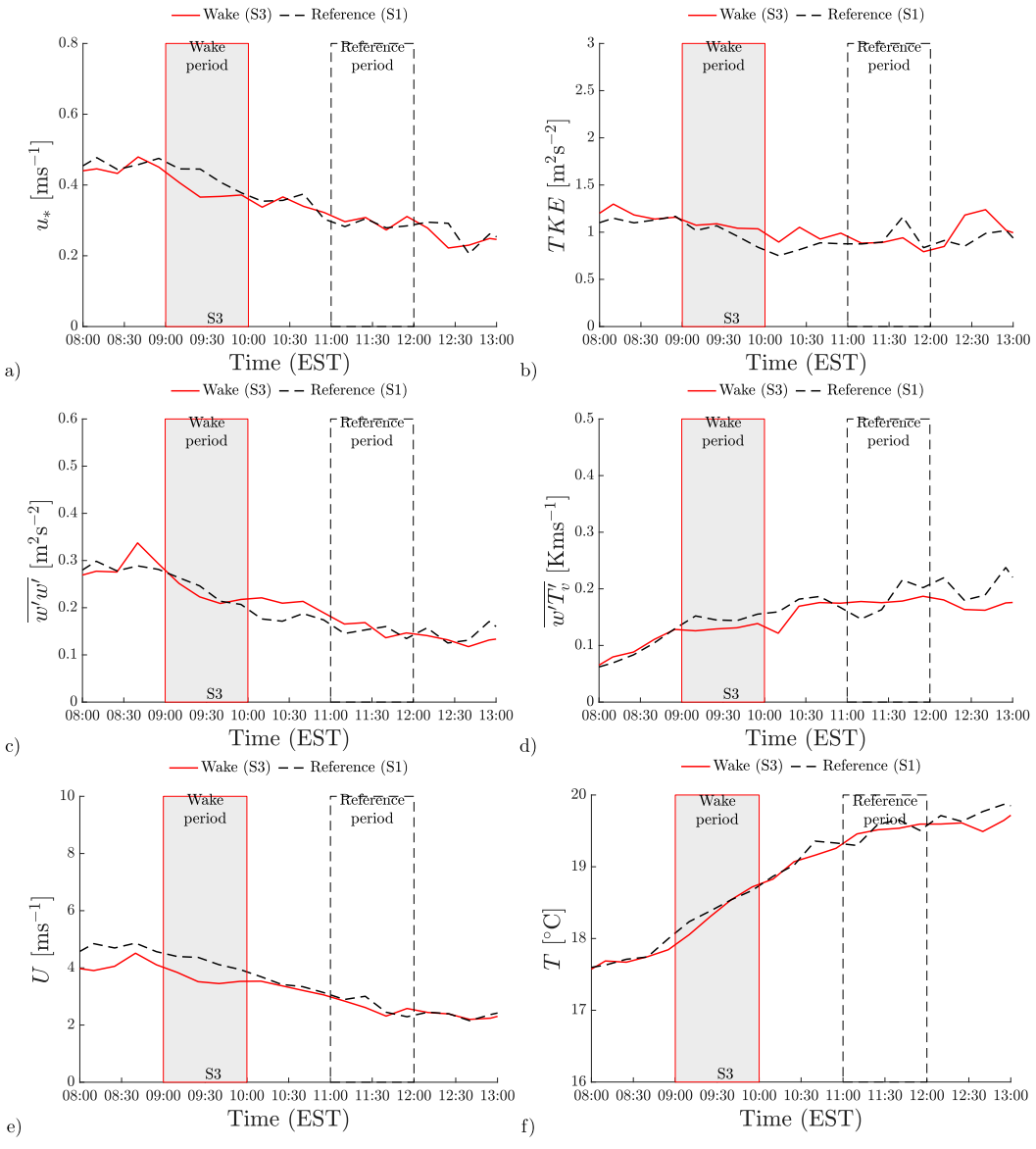

FIG. 6. As in Fig. 4, but for the unstable wake event of 25 Sep 2016.

the east afterward. The wake station was S3 and the reference station was S1. To guarantee the same stability between the reference period and the wake period, the reference period was selected from 1100 to 1200 EST when neither S3 nor S1 were under the wake, while the wake period was from 0900 to 1000 EST, with wake station S3 and reference station S1.

A reduction in u_* was found at the wake station S3 during the wake period (Fig. 6b), with mean normalized Δu_* decreasing from 0.03 ± 0.05 during the reference period to −0.09 ± 0.07 during the wake period. Similarly, horizontal wind speed U at the wake station S1 was higher than that at S3 before the wake but became lower than that at S3 after the wake arrival (Fig. 6f); the mean normalized difference was −0.02 ± 0.11 during the reference period and −0.15 ± 0.04 during the wake period. Although there was a slight increase in TKE, a decrease of $\overline{w'w'}$ was found. The temperature dropped slightly at S3 after the wake passage, but not significantly.

b. *Statistical analysis*

In this section, statistical significance will be reported using the Wilcoxon signed-rank test with a 95% confidence interval. The statistical analysis is based on the DiD approach, as described in section 3c, thus it will focus on pairs of stations: a wake station and a no-wake (or reference) station.

Figures 7–12 show the differences of normalized wind speed and friction velocity, heat flux, and temperature between wake and no-wake stations, grouped by atmospheric stability. Only the values in the shaded areas (i.e., no-wake northerly conditions in green and wake conditions in red) should be

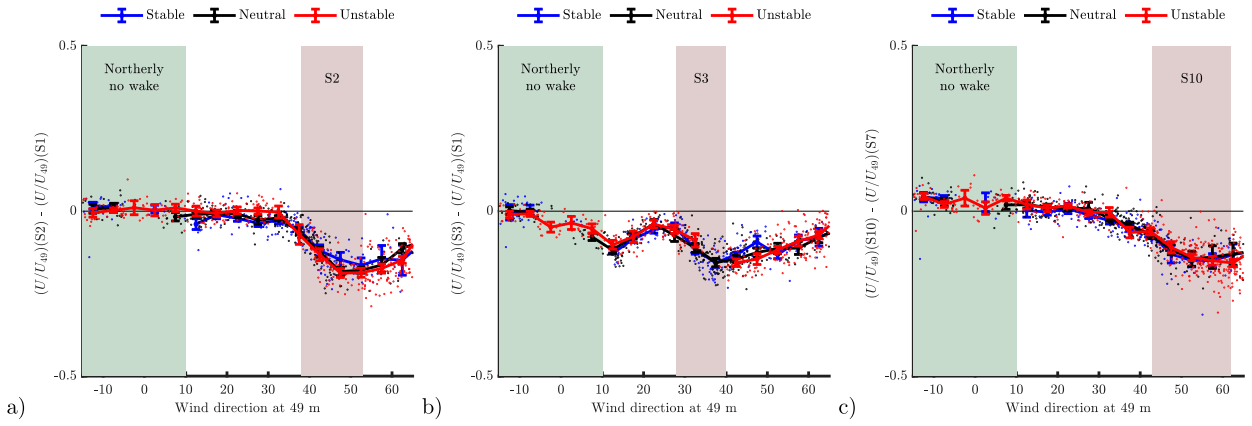

FIG. 7. Difference (mean and 95% confidence interval) between normalized 3-m horizontal wind speed at the wake station minus that at the no-wake station (a) S2 − S1, (b) S3 − S1, and (c) S10 − S7. The wind directions for which neither the wake nor the no-wake station is under wake are in the green-shaded areas, while those for which the wake station is under the wake are in the red-shaded areas.

considered, since we do not know the position of the wake or which site might be under it except for the wake and no-wake wind direction ranges. The sample size for the station pairs are listed in Table 3. The average values of the changes are reported in Tables 4–8.

Starting with 3-m wind speed for the close-wake stations S3 and S2 (Figs. 7a,b), the most noticeable feature is that the difference of normalized wind speed $\Delta U/U_{49}$ becomes negative in the red-shaded areas, while it is around zero in the green-shaded areas. Using the DiD approach, this means that the sites under the wake, S2 and S3, experience a reduction in wind speed when compared to the site outside of the wake, S1. The wind speed reduction is statistically significant and does not depend much on atmospheric stability (Table 4). Looking at wind speed at S2–S1, for example, the difference between the pair is around zero in the absence of a wake, meaning that the two sites experience the same wind speed when there is no wake (Fig. 7a). But the normalized difference becomes large and negative (−0.128 on average) when the wake hits S2 for stable and neutral conditions, indicating a reduction of wind speed at S2. We can conclude that the net effect is due to the wake because the sign of the difference is negative under the wake *and* it is near zero during no-wake conditions, thus only the turbine can be the reason.

The finding of reduced wind speed under the wake is consistent with the expansion of the wind speed deficit with distance in the wake. As the wind speed starts to recover farther downstream, the deficit is reduced, but the normalized wind speed reduction caused by the wake remains approximately the same at the distant-wake stations S10 (Fig. 7c), between −0.116 and −0.137 on average depending on stability, for a near-zero (or slightly positive) difference during no-wake conditions (Table 4).

The difference in normalized friction velocity at close-wake station pairs (Figs. 8a,b) exhibits the same behavior as $\Delta U/U_{49}$, with a clear decrease at the site under the wake during stable and neutral stability. The decrease in friction velocity under the wake is small in magnitude because it is normalized by a large value (U_{49}), but it is statistically significant and stronger for neutral than stable conditions (Table 5). For distant-wake stations, the decrease in friction velocity is almost negligible compared to that in the close-wake region (Fig. 8c), possibly due to the recovery of the wind turbine wake that causes wind shear below the rotor in the distant-wake to almost recover to the undisturbed value.

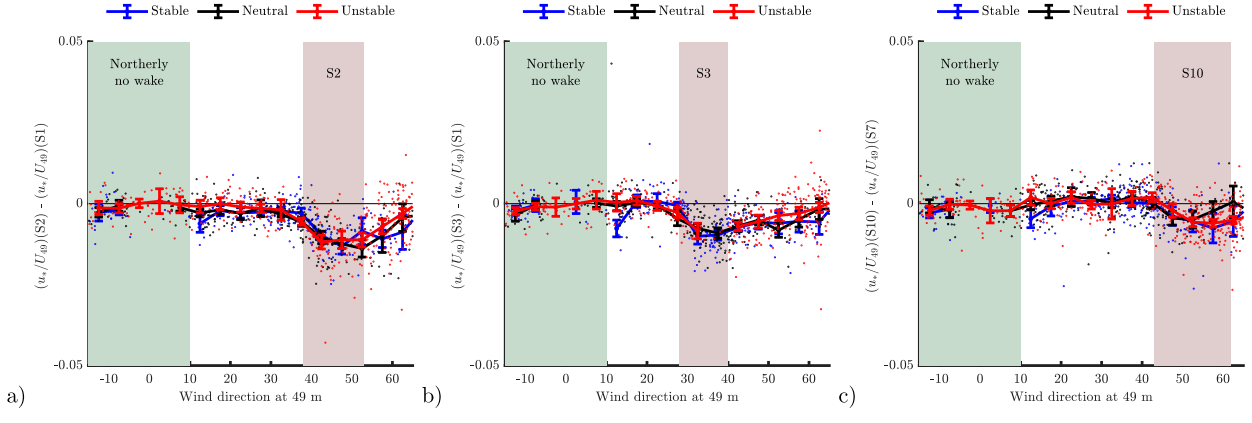

FIG. 8. As in Fig. 7, but for normalized friction velocity.

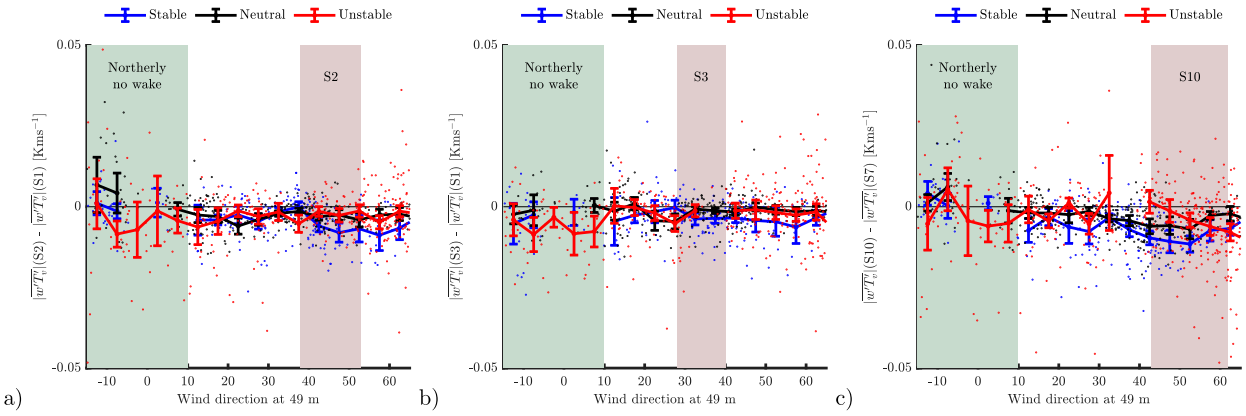

FIG. 9. As in Fig. 7, but for the magnitude of turbulent heat flux $|\overline{w'T'_v}|$.

While the findings so far—decreases of wind speed and friction velocity under the wake—have been clear to detect, easy to interpret physically, independent of atmospheric stability, and statistically significant, the next will be less straightforward.

Turbulent heat flux in the close-wake region (Figs. 9a,b) exhibits large fluctuations, especially during unstable conditions and in the absence of a wake. No obvious reduction or increase can be detected during stable conditions at S3. A significant reduction is apparent at S2 under stable conditions, although the magnitude is small (Table 6). Similarly, in the distant-wake station (Fig. 9c) there appears to be a significant reduction under stable conditions only (Table 6). On one hand, it is troublesome to reconcile the lack of significant changes in the heat flux when both wind speed and friction velocity experienced reductions. On the other hand, the same finding was also reported by Rajewski et al. (2013): "the data do not show a systematic and significant influence of the turbines" on the surface heat flux.

The efficiency of turbulent momentum exhibits a similar reduction as friction velocity under the wake for all stability conditions for close-wake stations (Figs. 10a,b). The reduction in distant-wake stations is much smaller compared to that of close-wake stations, and the statistical significance is lost for the S10–S7 pair under stable and neutral conditions (Fig. 10c). The DiD in turbulent transfer efficiency of heat has large fluctuations and does not show any meaningful differences (Figs. 11a–c).

For temperature, the changes caused by the wake are strongly dependent on atmospheric stability. At the close-wake sites, the strongest warming under the wake occurs in stable conditions (Figs. 12a,b). The magnitude of the warming induced by the wake is around +0.21 K on average and it is statistically significant for both close-wake station pairs (Table 8). In neutral conditions, a smaller but statistically significant warming is found at both S2 and S3. It is worth noting that the most significant warming occurs in stable conditions, during which no significant change in the heat flux was observed. Vice versa, in neutral conditions, the site that experienced a reduction in heat flux, S2, experienced a slight but statistically significant increase in temperature. This suggests that the temperature effects are, somehow, not linked to the surface heat flux, which drives local stability.

The temperature change in distant-wake pairs (Fig. 12c) are more complex. Only S10 shows a weak warming signal under stable conditions (Table 8), by approximately +0.11 K. At S10 a reduction of the heat flux was observed during stable

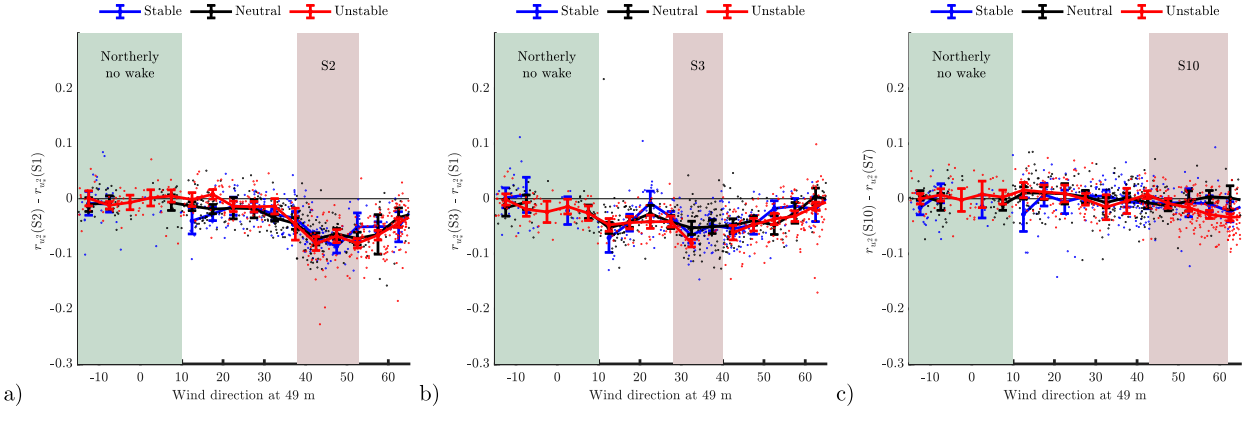

FIG. 10. As in Fig. 7, but for transfer efficiency of turbulent momentum r_{u*}.

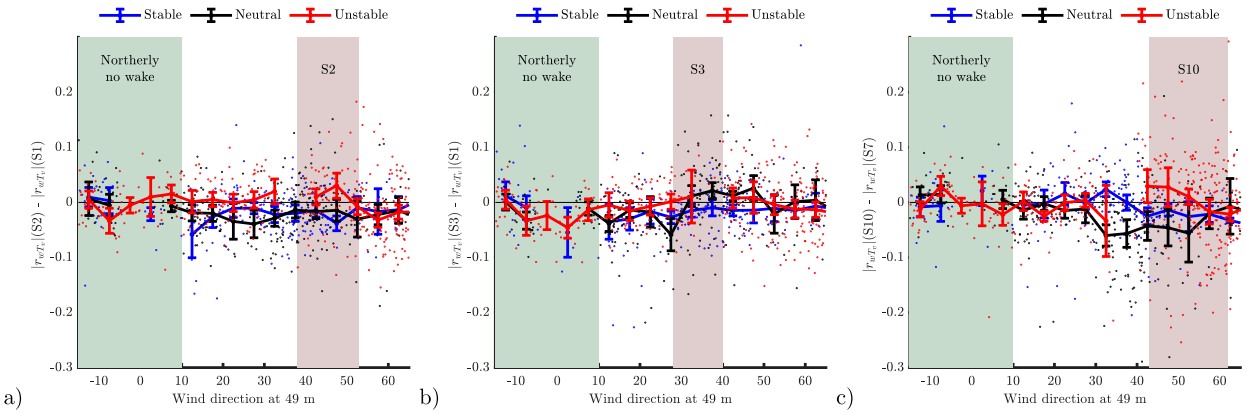

FIG. 11. As in Fig. 7, but for magnitude of transfer efficiency of heat $|r_{wT_v}|$.

conditions, which would cause cooling, not warming. Again, this further confirms that temperature effects by a wind turbine cannot be explained by surface heat fluxes.

We would like to point out that the temperature changes caused by the wind turbine wake, although statistically significant and unequivocally associated to the wake due to the DiD approach, are not large compared to natural variability, which can be estimated by the temperature differences between the pairs under no-wake conditions as ±0.09 on average (Table 8).

As changes in near-surface temperature do not seem to relate to changes in the surface heat flux, which is the parameter that drives traditional stability metrics (e.g., the Obukhov length L), we are going to investigate if they are correlated with the lower-rotor lapse rate Γ_{LR}.

The dependency of the changes in near-surface temperature caused by the wake on the lower-rotor lapse rate can be appreciated in Fig. 13 for the site pair S3–S1. No obvious relationship between stability and the temperature differences at S3–S1 can be found during no-wake conditions (i.e., northerly winds, Fig. 13a), when S3 is on average around 0.06 K cooler than S1. However, when the wake is over S3 (Fig. 13b), the response depends on stability. In unstable conditions, S3 is cooler than S1 by around 0.07 K, indicating that the temperature decrease caused by the wake is small and negligible. In neutral conditions, the difference in temperature between S3 and S1 is on average near zero in magnitude; comparing to the no-wake conditions, a slight warming signal is present. In stable conditions, there is a clear warming signal induced by the wake: on average, S3 is warmer than S1 by 0.1 K. The strongest warming is to be expected in the presence of an inversion and it could be up to 0.4 K.

In conclusion, the statistical analysis (Tables 4–8) of the VERTEX campaign data confirm that near the ground under a wind turbine wake:

- Vertical mixing is reduced, not enhanced, near the ground under the wake. Friction velocity u_* decreased significantly in all close-wake cases under all stabilities and in the distant-wake case for unstable conditions; no case with an increase of u_* was found.
- Wind speed is reduced near the ground under the wake. In all cases, for all stabilities and for all distances from the turbine, the horizontal wind speed decreased after the wake arrival with statistical significance.
- The surface heat flux is generally unaffected by the wake. The only statistically significant signal was a reduction in the heat flux during stable conditions at two of the three site pairs.
- Statistically significant (but modest in magnitude) warming was observed under stable conditions at all sites, by up

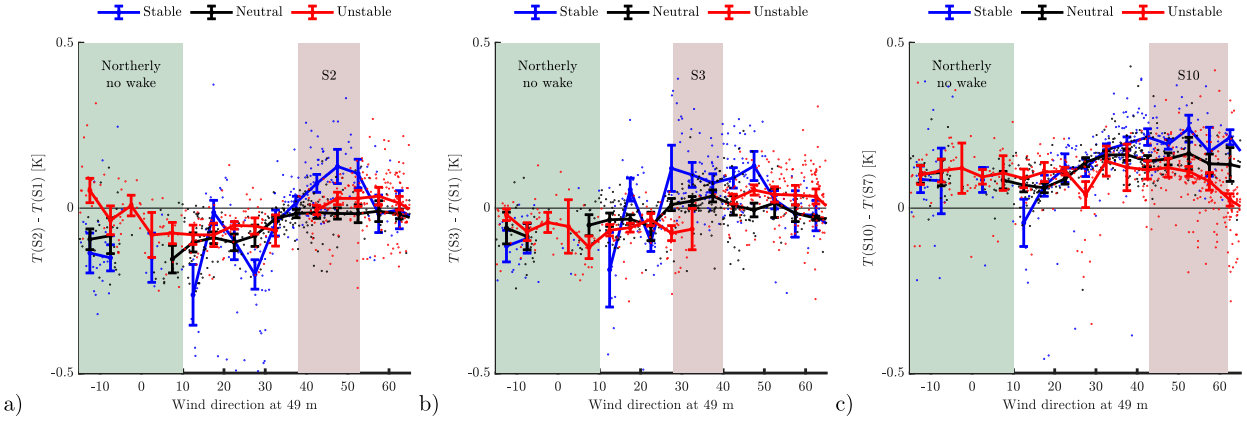

FIG. 12. As in Fig. 7, but for 2-m temperature.

TABLE 3. Sample size for the statistical analysis of DiD properties for northerly no-wake for all pairs, S2 under the wake in the S2–S1 pair, S3 under the wake in the S3–S1 pair, and S10 under the wake in the S10–S7 pair.

	Northerly no-wake	S2	S3	S10
Stable	32	68	66	51
Neutral	45	82	82	56
Unstable	61	80	19	172

to +0.4 K. Slight warming under neutral conditions was also found in the close wake. Temperature changes are better correlated with stability assessed with the lower-rotor lapse rate Γ_{LR} than with surface heat fluxes.

These findings give rise to a challenging question: how can warming occur near the surface without a change in the surface heat flux? Many modeling studies in the literature have reported changes in near-surface temperature caused by changes in the surface heat fluxes. In the next section we attempt to provide an answer to this question.

5. Discussion

The mechanism behind the reduction of vertical mixing under the wake has already been explained in Archer et al. (2019) and is only summarized here. The extraction of kinetic energy by the wind turbine causes a wind speed deficit at the rotor area that propagates farther downwind. The wind speed deficit alters the vertical wind shear profile and causes an enhancement of shear above hub height and negative shear below it. The upward transfer of momentum from the bottom of the wake to the hub height ''sucks in'' the higher momentum below the wake. Consequently, wind shear is reduced below the wake, causing a reduction of shear and shear-production of turbulence, which is one of the drivers of vertical mixing. The results are in agreement with wind tunnel studies (Chamorro and Porté-Agel 2010) and LES studies (Xie and Archer 2017).

Although no information on turbulence in the upper wake is available in VERTEX, we propose that the reduction of shear caused by the reduction of wind speed is the dominant factor that drives changes of vertical mixing near the ground, at least in stable and neutral stratified atmospheres. The enhancement of mixing only occurs above the hub height and is caused by the combination of direct blade-induced turbulence and indirect increase in wind shear (Lu and Porté-Agel 2011; Calaf et al. 2011; Xie and Archer 2017). With this information at hand, i.e., a wind turbine wake with high turbulence only in its upper part and a wind speed deficit that reaches the ground, in this section we will try to explain how near-surface temperature changes can take place.

To understand how warming/cooling can occur near the surface without a change in the surface heat flux, we propose here that the warming/cooling near the surface, where vertical mixing is reduced, is controlled by the changes in the divergence (or convergence) of the heat fluxes below the rotor, despite constant or slightly reduced surface heat fluxes and despite reduction in turbulence production due to reduced wind shear.

The theoretical justification for this mechanism lies in the energy equation, assuming horizontal homogeneity [Stull 1988, Eq. (3.4.5b)] and neglecting the changes of pressure following the air parcels [Gill 1982, Eq. (4.4.7)]:

$$\overline{\rho}C_p\frac{\partial\overline{T}}{\partial t}=-\overline{\rho}C_p\left(\overline{w}\frac{\partial\overline{T}}{\partial z}+\frac{\partial\overline{w'T'}}{\partial z}\right)+\frac{\partial Q_{\mathrm{rad}}}{\partial z}+Q_H\,. \qquad (7)$$

The first term on the right-hand side is the vertical advection of temperature and the second term is the vertical divergence of turbulent heat flux (with a minus sign to indicate that convergence causes warming). The other two terms are radiative heating (Q_{rad}) and the combined effect of viscous dissipation and latent heat (Q_H), which we can ignore as a first approximation, leaving the vertical advection and the divergence of heat flux as the two possible mechanisms controlling the temperature change near the ground. The importance of these two terms was proposed first by Xia et al. (2019), who concluded from numerical simulations that they both play a role in the temperature changes near the ground downwind of inland wind farms.

In VERTEX, the vertical advection of temperature was not found to be an important factor. It was estimated with vertical wind speed measured at 3 m and virtual temperature gradient between 10 and 7 m. For both close- and distant-wake stations, vertical advection did not show a distinguishable signal when the station was under the wake (not shown), compared to northerly wind when no station was under the wake. As such, we focus on the vertical divergence of heat flux only in the rest of the section.

TABLE 4. Results of the statistical analysis: difference of 3-m horizontal wind speed between wake and no-wake sites (i.e., S2 − S1 and S3 − S1 in the close-wake region, S10 − S7 in the distant-wake region), normalized by wind speed at 49 m. Statistically significant ($p < 0.01$) results for wake conditions are in boldface for decreases and in boldface and italic for increases. The values reported are means with standard deviations in parentheses.

U/U_{49}(Wake) − U/U_{49}(Ref)		S2 − S1	S3 − S1	S10 − S7
No-wake conditions	Stable	0.006 (0.032)	−0.012 (0.042)	0.032 (0.039)
	Neutral	−0.001 (0.028)	−0.030 (0.043)	0.027 (0.029)
	Unstable	0.003 (0.026)	−0.031 (0.029)	0.031 (0.029)
Wake conditions	Stable	**−0.123 (0.053)**	**−0.126 (0.051)**	**−0.125 (0.055)**
	Neutral	**−0.132 (0.056)**	**−0.128 (0.048)**	**−0.116 (0.052)**
	Unstable	**−0.156 (0.051)**	**−0.090 (0.037)**	**−0.137 (0.053)**

TABLE 5. As in Table 4, but for normalized friction velocity.

u_*/U_{49}(Wake) − u_*/U_{49}(Ref)		S2 − S1	S3 − S1	S10 − S7
No-wake conditions	Stable	−0.002 (0.004)	−0.001 (0.005)	−0.002 (0.003)
	Neutral	−0.002 (0.003)	−0.001 (0.003)	−0.002 (0.004)
	Unstable	−0.001 (0.004)	−0.001 (0.004)	−0.001 (0.004)
Wake conditions	Stable	**−0.010 (0.006)**	**−0.008 (0.006)**	−0.004 (0.007)
	Neutral	**−0.010 (0.006)**	**−0.008 (0.005)**	−0.002 (0.006)
	Unstable	**−0.012 (0.007)**	**−0.007 (0.004)**	**−0.005 (0.005)**

Evidence from LES results in the literature (Lu and Porté-Agel 2011; Calaf et al. 2011; Xie and Archer 2017) suggests that two main processes affect vertical mixing within the rotor area of a wake: 1) an increase in wind shear due to the wind speed deficit in the upper part of the rotor area (above hub height) and 2) added TKE due to the rotation of the blades and the formation of tip vortices in the entire rotor area. As a result of these two mechanisms, large TKE increases are found in the upper part of the rotor area (above hub height) and modest increases in the lower part of the wake, i.e., below hub height but above the bottom tips. These two effects are sketched in Fig. 14 as large swirls in the upper part of the wake and smaller swirls in the lower part. From the previous VERTEX results, we know that vertical mixing near the surface is reduced, thus no swirls are shown below the wake. The heat fluxes are represented as arrows, pointing upward in unstable conditions and downward in stable conditions, or as "0" in neutral conditions. The mean wind flow is left to right, thus the undisturbed heat fluxes are to the left of the turbine and the altered heat fluxes due to the turbine wake are to the right. Blue and green are used to indicate two slightly different potential temperature profiles, found during VERTEX, within the same general stability category.

In stable conditions (Fig. 14a), with or without a ground-based inversion (blue and green lines, respectively), the upstream downward heat fluxes are largest near the ground and decrease nearly linearly with height (Stull 1988, Fig. 2.15). This distribution results in a slight divergence of the heat fluxes at all levels. The combination of enhanced mixing in the wake and unchanged or slightly reduced surface heat flux causes a convergence of the heat fluxes below the rotor. Consequently, warming is expected near the ground. Note that, if only the surface heat fluxes were considered, cooling or no change would be expected as a consequence of the slightly reduced or unaffected downward surface heat fluxes.

In unstable conditions (Fig. 14b), with a deep or shallow superadiabatic layer (blue and green lines, respectively), the upstream upward heat fluxes are largest near the ground and decrease linearly with height (Stull 1988, Fig. 2.15). Note that the convective well-mixed layer is characterized by an adiabatic lapse rate but also by upward heat fluxes (Stull 1988, Figs. 2.15 and 3.7). This distribution results in a slight convergence of the heat fluxes at all levels. Below the rotor, the exact thermal response depends on the thickness of the superadiabatic layer. If it is deep enough to intersect the rotor region (blue line), then a reduction of convergence or even divergence may occur instead of convergence and cooling is expected near the ground; if it is shallow (green line), then the previous convergence may just be slightly reduced, causing slight or no cooling at the surface.

In neutral conditions (Fig. 14c), the upstream heat fluxes are near zero all the way to the capping stable level. There will be no change in near-surface temperature if the stable layer is above the rotor (blue line). However, if there is a stable layer that intersects the rotor area (green line), e.g., during the erosion of the nocturnal ground-based inversion after sunrise, the mixing by the turbine will slightly enhance the downward heat flux, increasing convergence below the rotor. In this case there will be warming near the ground.

Direct evidence of the heat flux divergence mechanism could not be gathered during the VERTEX cases because the met tower, although it measured heat fluxes at five levels below hub height, was located upstream of the turbine, not downstream, during the northeasterly wake events. However, when the wind was from the southwest, the met tower was likely to be under the wake. It was therefore possible to estimate the heat flux divergence using the gradient of the heat flux between the top height (49 m) and the lowest height (10 m) of the met tower:

$$\frac{\partial \overline{w'T_v'}}{\partial z} \approx \frac{\Delta \overline{w'T_v'}}{\Delta z} = \frac{\overline{w'T_{v49}'} - \overline{w'T_{v10}'}}{49\,\mathrm{m} - 10\,\mathrm{m}}. \tag{8}$$

The time periods when the met tower was hit by the wake were determined using the wake detection algorithm from section 4b,

TABLE 6. As in Table 4, but for the magnitude of turbulent heat flux $|\overline{w'T_v'}|$.

$\lvert\overline{w'T_v'}\rvert$(Wake) − $\lvert\overline{w'T_v'}\rvert$(Ref) (K m^{-1})		S2 − S1	S3 − S1	S10 − S7
No-wake conditions	Stable	0.000 (0.007)	−0.005 (0.013)	0.002 (0.007)
	Neutral	0.003 (0.010)	−0.002 (0.009)	0.003 (0.010)
	Unstable	−0.004 (0.016)	−0.009 (0.013)	−0.003 (0.014)
Wake conditions	Stable	**−0.006 (0.006)**	−0.003 (0.005)	**−0.010 (0.006)**
	Neutral	**−0.002 (0.004)**	−0.002 (0.004)	**−0.005 (0.005)**
	Unstable	−0.003 (0.005)	−0.007 (0.008)	−0.006 (0.013)

TABLE 7. As in Table 4, but for turbulent transfer efficiency of momentum r_{u*}.

r_{u*}(wake) − r_{u*}(ref)		S2 − S1	S3 − S1	S10 − S7
No-wake conditions	Stable	−0.010 (0.042)	−0.005 (0.042)	−0.008 (0.034)
	Neutral	−0.008 (0.024)	−0.016 (0.026)	−0.005 (0.026)
	Unstable	−0.004 (0.027)	−0.017 (0.028)	0.004 (0.027)
Wake conditions	Stable	**−0.067 (0.033)**	**−0.052 (0.033)**	−0.008 (0.034)
	Neutral	**−0.067 (0.032)**	**−0.051 (0.036)**	−0.007 (0.031)
	Unstable	**−0.080 (0.038)**	**−0.061 (0.025)**	**−0.020 (0.027)**

but for southwesterly wind directions. During VERTEX, a total of five time periods in which the tower was likely to be hit by a wake occurred, shown in Fig. 15.

The first case, characterized by very stable conditions with a temperature inversion, lasted from 1945 EST 8 September to 0300 EST 9 September (shading in Fig. 15a). At first, $\Delta\overline{w'T_v'}/\Delta z$ was positive around $2\,\mathrm{K\,h^{-1}}$, which is consistent with the gradually decreasing negative heat flux with height. However, starting at approximately 1945 EST, the divergence of the heat flux dropped dramatically from positive to negative (thus convergence), likely as a response to the arrival of the wake, and eventually oscillated between -2 and $-4\,\mathrm{K\,h^{-1}}$. From 0300 EST, when the wake moved away from the tower, the divergence recovered to a slightly positive value.

The second case, characterized by a near-neutral lapse rate, lasted from 0200 EST 27 September to 0500 EST 27 September (shading in Fig. 15b). The divergence of the turbulent heat flux changed from near-zero to slightly negative (thus weak convergence) more gradually. The other three periods behaved similarly (Figs. 15c–e). The observed changes in the divergence of the heat flux when the met tower was under the wake provide preliminary evidence of the existence and coherence of this mechanism in driving temperature changes near the ground.

6. Conclusions

The VERTEX field campaign aims at answering two research questions: (i) What is the impact of wind turbine wakes on vertical mixing, wind speed, and temperature near the ground? (ii) What physical mechanisms are responsible for the observed changes?

We have observed the following near the surface under the wind turbine wake:

1) A reduction of vertical mixing and wind speed, which are caused by the reduction of wind shear near the ground, caused in turn by the momentum deficit in the wake;
2) A lack of change in surface turbulent heat flux and moisture;
3) Small temperature changes (lower than 0.4°C in magnitude, on average comparable in magnitude with the natural variability in the marsh) but statistically significant; and
4) A correlation of near-ground temperature changes with the lower-rotor lapse rate.

The proposed mechanism that drives the changes in near-ground temperature by wind turbine wakes is the change in the vertical divergence/convergence of turbulent heat flux below the rotor. This mechanism may cause the following under single wind turbine wakes, depending on the lower-rotor lapse rate:

- Under stable conditions, the enhanced downward heat flux in the lower-rotor region and the lack of change in surface heat flux cause a convergence in heat flux below the rotor, which causes an increase in the near-surface temperature;
- Under unstable conditions, the change in vertical convergence of heat flux depends on the depth of the superadiabatic surface layer: with a deep superadiabatic layer, less convergence or even divergence of heat flux occurs below the rotor, instead of the previous convergence, which decreases the surface temperature; with a shallow layer (more common), the convergence is slightly reduced below the rotor, which may cause a slight cooling or no significant effect;
- Under neutral conditions, no change is expected in temperature near the ground. An exception may occur when the neutral layer is topped by a stable layer that intersects the rotor layer, in which case a slight warming may occur near the ground due to enhanced heat flux convergence.

The lack of correlation between near-surface temperature changes and surface heat fluxes and the positive correlation between near-surface temperature changes and the lower-rotor lapse rate suggest that the prediction of near-surface temperature changes caused by wind farms depend on the vertical temperature structure from the ground to the rotor region. The lower-rotor lapse rate is an effective metric for multiple reasons.

TABLE 8. As in Table 4, but for 2-m temperature.

T(wake) − T(ref) (K)		S2 − S1	S3 − S1	S10 − S7
No-wake conditions	Stable	−0.12 (0.12)	−0.11 (0.12)	0.08 (0.15)
	Neutral	−0.11 (0.09)	−0.07 (0.07)	0.10 (0.08)
	Unstable	−0.01 (0.10)	−0.06 (0.07)	0.11 (0.11)
Wake conditions	Stable	***0.09 (0.09)***	***0.10 (0.10)***	***0.19 (0.15)***
	Neutral	***−0.01 (0.06)***	***0.02 (0.06)***	***0.15 (0.06)***
	Unstable	0.00 (0.07)	−0.07 (0.08)	0.09 (0.10)

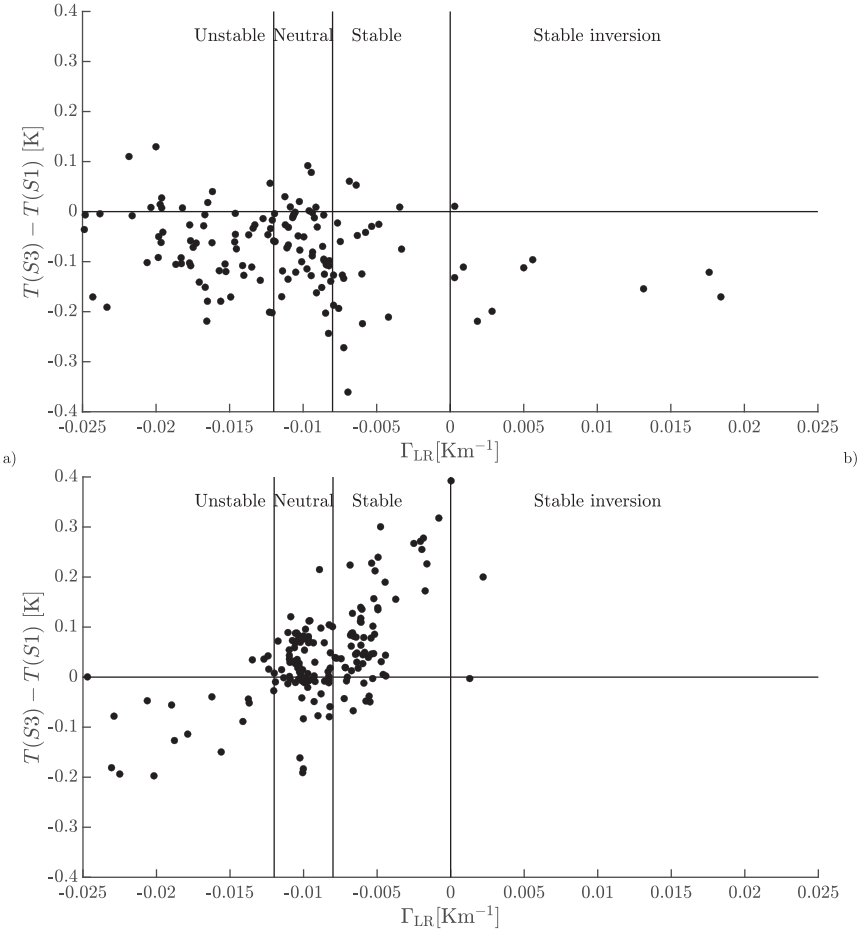

FIG. 13. Near-surface (2 m) temperature difference between S3 and S1 as a function of the lower-rotor lapse rate Γ_{LR} between the 49- and 10-m levels of the met tower for (a) (northerly) no-wake conditions and (b) wake conditions at S3 (i.e., with wind directions such that S3 is under the wake, while S1 is not).

First, the stability in the rotor region—especially in the lower part—is the driving factor for the convergence/divergence mechanism, because it determines the sign of the enhanced fluxes, either upward or downward. Although necessary, the stability in the rotor region alone would not be sufficient. Let us consider for example the case of an unstable boundary layer with a shallow superadiabatic layer followed by a neutral convective layer across the rotor. If the rotor stability were the only metrics, we would wrongfully conclude that the boundary layer is neutral and therefore expect no change in surface temperature. This suggests that information on surface stability should be utilized too, but not alone either. For example, during the erosion of the nocturnal ground-based inversion after sunrise, neutral or unstable conditions may occur near the ground, while the rotor region is still stable. If only surface stability was known, cooling or no change in near-surface temperature would be wrongfully predicted. In summary, the lower-rotor lapse rate can properly account for both rotor and surface stability. In VERTEX, it allowed us to correctly predict warming and cooling near the surface in most cases. The only exceptions were a few wake cases that were classified as neutral according to the lower-rotor lapse rate but were associated with slight warming, likely because the stable layer on top of the neutral layer was above 49 m. We suspect that one of the main reasons why past studies, including field campaigns, reported some inconsistencies between the observed temperature changes and the associated atmospheric stability was that they either used surface stability or a simple day/night characterization of stability. The former is incorrect because it neglects the rotor layer and the latter because it implicitly assumes that the atmosphere is stable at night and unstable during the day, whereas it can often be stable or neutral during the day. In fact, studies that used a day/night characterization of stability often found a lack of cooling or even a warming signal during the day, which would be impossible to explain with enhanced vertical mixing near the ground and were likely just days with a stable or neutral rotor-layer lapse rate.

A limitation of the VERTEX field campaign is that the measurements of mixing properties and climatological properties were conducted under the wake of a single wind turbine only. For larger wind farms, nonlinear interactions

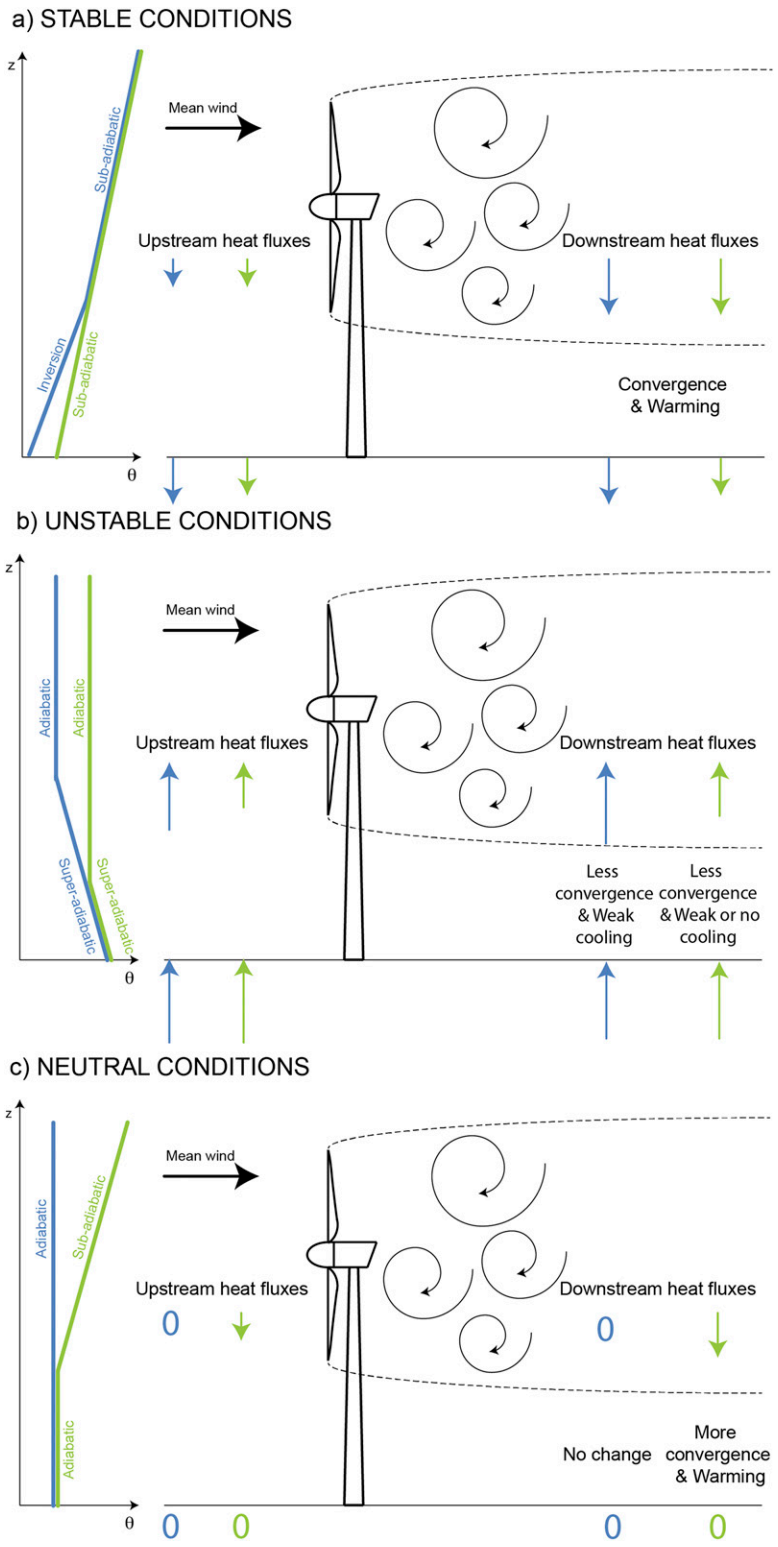

FIG. 14. The proposed mechanism to explain changes in near-surface temperature based on the changes in divergence/convergence of the heat fluxes below the rotor during: (a) stable, (b) unstable, and (c) neutral atmospheric stability. In green and blue are two typical upstream conditions found in VERTEX per stability category, for both potential temperature and heat flux profiles. The swirls represent the added TKE and enhanced vertical mixing caused by the wake within the rotor area, which are stronger in the upper part of the rotor than below hub height based on the literature.

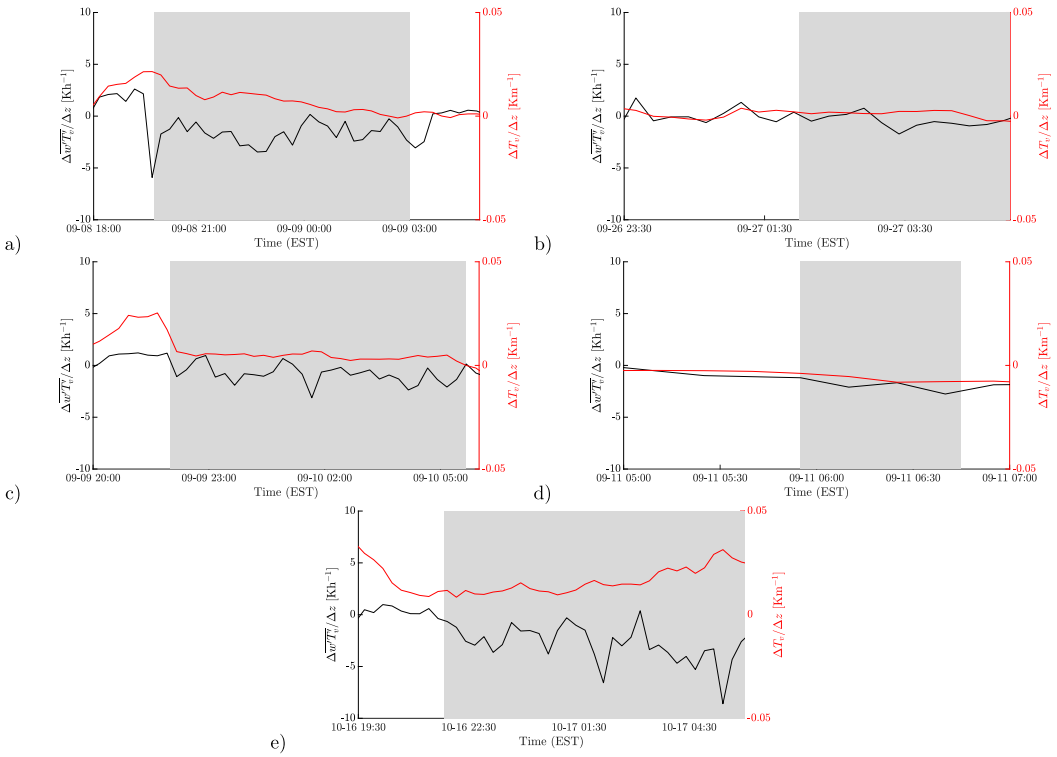

FIG. 15. Divergence of turbulent heat flux between the 49- and 10-m levels of the met tower (black line) and the lower-rotor lapse rate (red line) under the influence of the wake (gray shading) during (a) 1945 EST 8 Sep to 0300 EST 9 Sep; (b) 0200 EST 26 Sep–0500 EST 27 Sep; (c) 2200 EST 9 Sep–0540 EST 10 Sep; (d) 0555–0645 EST 11 Sep; and (e) 2150 EST 16 Oct–0600 EST 17 Oct.

by the overlapping wakes may cause different impacts on vertical mixing and temperature near the ground (Ghaisas et al. 2017). Also, the surface flux stations were located in a marsh downwind of the turbine, thus the findings from the VERTEX campaign may or may not be representative of low- to medium-humidity conditions at inland locations. In addition, the lack of effects on moisture may be due to the fact that relative humidity was generally high during the campaign and therefore any changes caused by the turbine wake may not have been large enough to be detected over noise.

In future studies, we will conduct single-turbine, high-resolution, idealized simulations under a variety of incoming boundary conditions, such as different vertical temperature profiles across the rotor (stable, stable with ground-based inversions, etc.), moisture, wind speeds, among others. In-line coupling with a land surface model will ensure that the feedback between the atmosphere and the soil is properly captured (e.g., with the WRF Model).

Acknowledgments. The authors report no conflicts of interest. Funding for this research was provided by the National Science Foundation (Award 1564565).

Data availability statement. The meteorological data collected during the VERTEX field campaign are available at https://www.eol.ucar.edu/field_projects/vertex (click on "Data access" in the menu on the right).

REFERENCES

Archer, C. L., B. A. Colle, D. L. Veron, F. Veron, and M. J. Sienkiewicz, 2016: On the predominance of unstable atmospheric conditions in the marine boundary layer offshore of the U.S. northeastern coast. *J. Geophys. Res. Atmos.*, **121**, 8869–8885, https://doi.org/10.1002/2016JD024896.

——, S. Wu, A. Vasel-Be-Hagh, J. F. Brodie, R. Delgado, A. St. Pé, S. Oncley, and S. Semmer, 2019: The vertex field campaign: Observations of near-ground effects of wind turbine wakes. *J. Turbul.*, **20**, 64–92, https://doi.org/10.1080/14685248.2019.1572161.

——, ——, Y. Ma, and P. A. Jiménez, 2020: Two corrections for turbulent kinetic energy generated by wind farms in the WRF Model. *Mon. Wea. Rev.*, **148**, 4823–4835, https://doi.org/10.1175/MWR-D-20-0097.1.

Armstrong, A., R. R. Burton, S. E. Lee, S. Mobbs, N. Ostle, V. Smith, S. Waldron, and J. Whitaker, 2016: Ground-level climate at a peatland wind farm in Scotland is affected by wind turbine operation. *Environ. Res. Lett.*, **11**, 044024, https://doi.org/10.1088/1748-9326/11/4/044024.

Baidya Roy, S., and J. J. Traiteur, 2010: Impacts of wind farms on surface air temperatures. *Proc. Natl. Acad. Sci. USA*, **107**, 17 899–17 904, https://doi.org/10.1073/pnas.1000493107.

——, S. W. Pacala, and R. L. Walko, 2004: Can large wind farms affect local meteorology? *J. Geophys. Res.*, **109**, D19101, https://doi.org/10.1029/2004JD004763.

Barrie, D. B., and D. B. Kirk-Davidoff, 2010: Weather response to a large wind turbine array. *Atmos. Chem. Phys.*, **10**, 769–775, https://doi.org/10.5194/acp-10-769-2010.

Barthelmie, R. J., and Coauthors, 2010: Quantifying the impact of wind turbine wakes on power output at offshore wind farms. *J. Atmos. Oceanic Technol.*, **27**, 1302–1317, https://doi.org/10.1175/2010JTECHA1398.1.

Bodini, N., D. Zardi, and J. K. Lundquist, 2017: Three-dimensional structure of wind turbine wakes as measured by scanning lidar. *Atmos. Meas. Tech.*, **10**, 2881–2896, https://doi.org/10.5194/amt-10-2881-2017.

Calaf, M., C. Meneveau, and J. Meyers, 2010: Large eddy simulation study of fully developed wind-turbine array boundary layers. *Phys. Fluids*, **22**, 015110, https://doi.org/10.1063/1.3291077.

——, M. B. Parlange, and C. Meneveau, 2011: Large eddy simulation study of scalar transport in fully developed wind-turbine array boundary layers. *Phys. Fluids*, **23**, 126603, https://doi.org/10.1063/1.3663376.

Chamorro, L. P., and F. Porté-Agel, 2010: Effects of thermal stability and incoming boundary-layer flow characteristics on wind-turbine wakes: A wind-tunnel study. *Bound.-Layer Meteor.*, **136**, 515–533, https://doi.org/10.1007/s10546-010-9512-1.

Fitch, A. C., 2015: Climate impacts of large-scale wind farms as parameterized in a global climate model. *J. Climate*, **28**, 6160–6180, https://doi.org/10.1175/JCLI-D-14-00245.1.

——, 2016: Notes on using the mesoscale wind farm parameterization of Fitch et al. (2012) in WRF. *Wind Energy*, **19**, 1757–1758, https://doi.org/10.1002/we.1945.

——, J. B. Olson, J. K. Lundquist, J. Dudhia, A. K. Gupta, J. Michalakes, and I. Barstad, 2012: Local and mesoscale impacts of wind farms as parameterized in a mesoscale NWP model. *Mon. Wea. Rev.*, **140**, 3017–3038, https://doi.org/10.1175/MWR-D-11-00352.1.

Ghaisas, N., C. Archer, S. Xie, S. Wu, and E. Maguire, 2017: Evaluation of layout and atmospheric stability effects in wind farms using large-eddy simulation. *Wind Energy*, **20**, 1227–1240, https://doi.org/10.1002/we.2091.

Gill, A., 1982: *Atmosphere-Ocean Dynamics*. Academic Press, 662 pp.

Harris, R. A., L. Zhou, and G. Xia, 2014: Satellite observations of wind farm impacts on nocturnal land surface temperature in Iowa. *Remote Sens.*, **6**, 12 234–12 246, https://doi.org/10.3390/rs61212234.

Jacobson, M. Z., and C. L. Archer, 2012: Saturation wind power potential and its implications for wind energy. *Proc. Natl. Acad. Sci. USA*, **109**, 15 679–15 684, https://doi.org/10.1073/pnas.1208993109.

Keith, D. W., J. F. DeCarolis, D. C. Denkenberger, D. H. Lenschow, S. L. Malyshev, S. Pacala, and P. J. Rasch, 2004: The influence of large-scale wind power on global climate. *Proc. Natl. Acad. Sci. USA*, **101**, 16 115–16 120, https://doi.org/10.1073/pnas.0406930101.

Lu, H., and F. Porté-Agel, 2011: Large-eddy simulation of a very large wind farm in a stable atmospheric boundary layer. *Phys. Fluids*, **23**, 065101, https://doi.org/10.1063/1.3589857.

Miller, L. M., and D. W. Keith, 2018: Climatic impacts of wind power. *Joule*, **2**, 2618–2632, https://doi.org/10.1016/j.joule.2018.09.009.

Moravec, D., V. Barták, V. Puš, and J. Wild, 2018: Wind turbine impact on near-ground air temperature. *Renewable Energy*, **123**, 627–633, https://doi.org/10.1016/j.renene.2018.02.091.

Oncley, S. P., C. A. Friehe, J. C. Larue, J. A. Businger, E. C. Itsweire, and S. S. Chang, 1996: Surface layer fluxes profiles and turbulence measurements over uniform terrain under near neutral conditions. *J. Atmos. Sci.*, **53**, 1029–1044, https://doi.org/10.1175/1520-0469(1996)053<1029:SLFPAT>2.0.CO;2.

Pryor, S. C., R. J. Barthelmie, and T. J. Shepherd, 2018: The influence of real-world wind turbine deployments on local to mesoscale climate. *J. Geophys. Res. Atmos.*, **123**, 5804–5826, https://doi.org/10.1029/2017JD028114.

——, T. J. Shepherd, R. J. Barthelmie, A. N. Hahmann, and P. Volker, 2019: Wind farm wakes simulated using WRF. *J. Phys. Conf. Ser.*, **1256**, 012025, https://doi.org/10.1088/1742-6596/1256/1/012025..

Rajewski, D. A., and Coauthors, 2013: Crop Wind Energy Experiment (CWEX): Observations of surface-layer, boundary layer, and mesoscale interactions with a wind farm. *Bull. Amer. Meteor. Soc.*, **94**, 655–672, https://doi.org/10.1175/BAMS-D-11-00240.1.

——, E. S. Takle, J. K. Lundquist, J. H. Prueger, R. L. Pfeiffer, J. L. Hatfield, K. K. Spoth, and R. K. Doorenbos, 2014: Changes in fluxes of heat, H_2O, and CO_2 caused by a large wind farm. *Agric. For. Meteor.*, **194**, 175–187, https://doi.org/10.1016/j.agrformet.2014.03.023.

——, ——, J. H. Prueger, and R. K. Doorenbos, 2016: Toward understanding the physical link between turbines and microclimate impacts from in situ measurements in a large wind farm. *J. Geophys. Res. Atmos.*, **121**, 13 392–13 414, https://doi.org/10.1002/2016JD025297.

Roth, M., and T. R. Oke, 1995: Relative efficiencies of turbulent transfer of heat, mass, and momentum over a patchy urban surface. *J. Atmos. Sci.*, **52**, 1863–1874, https://doi.org/10.1175/1520-0469(1995)052<1863:REOTTO>2.0.CO;2.

Schotanus, P., F. T. Nieuwstadt, and H. A. De Bruin, 1983: Temperature measurement with a sonic anemometer and its application to heat and moisture fluxes. *Bound.-Layer Meteor.*, **26**, 81–93, https://doi.org/10.1007/BF00164332.

Sievers, J., T. Papakyriakou, S. E. Larsen, M. M. Jammet, S. Rysgaard, M. K. Sejr, and L. L. Sørensen, 2015: Estimating surface fluxes using eddy covariance and numerical ogive optimization. *Atmos. Chem. Phys.*, **15**, 2081–2103, https://doi.org/10.5194/acp-15-2081-2015.

Smith, C. M., R. J. Barthelmie, and S. C. Pryor, 2013: In situ observations of the influence of a large onshore wind farm on near-surface temperature, turbulence intensity and wind speed profiles. *Environ. Res. Lett.*, **8**, 034006, https://doi.org/10.1088/1748-9326/8/3/034006.

Stull, R. B., 1988: *An Introduction to Boundary Layer Meteorology*. Springer, 670 pp.

Sun, H., Y. Luo, Z. Zhao, and R. Chang, 2018: The impacts of Chinese wind farms on climate. *J. Geophys. Res. Atmos.*, **123**, 5177–5187, https://doi.org/10.1029/2017JD028028.

Volker, P. J., J. Badger, A. N. Hahmann, and S. Ott, 2015: The explicit wake parametrisation V1.0: A wind farm parametrisation in the mesoscale model WRF. *Geosci. Model Dev.*, **8**, 3715–3731, https://doi.org/10.5194/gmd-8-3715-2015.

Wang, C., and R. G. Prinn, 2010: Potential climatic impacts and reliability of very large-scale wind farms. *Atmos. Chem. Phys.*, **10**, 2053–2061, https://doi.org/10.5194/acp-10-2053-2010.

Wang, H., and R. J. Barthelmie, 2015: Wind turbine wake detection with a single Doppler wind lidar. *J. Phys. Conf. Ser.*, **625**, 012017, https://doi.org/10.1088/1742-6596/625/1/012017.

Xia, G., L. Zhou, J. M. Freedman, S. B. Roy, R. A. Harris, and M. C. Cervarich, 2016: A case study of effects of atmospheric boundary layer turbulence, wind speed, and stability on wind farm induced temperature changes using observations from a field campaign. *Climate Dyn.*, **46**, 2179–2196, https://doi.org/10.1007/s00382-015-2696-9.

——, ——, J. R. Minder, R. G. Fovell, and P. A. Jimenez, 2019: Simulating impacts of real-world wind farms on land surface temperature using the WRF model: Physical mechanisms. *Climate Dyn.*, **53**, 1723–1739, https://doi.org/10.1007/s00382-019-04725-0.

Xie, S., and C. L. Archer, 2015: Self-similarity and turbulence characteristics of wind turbine wakes via large-eddy simulation. *Wind Energy*, **18**, 1815–1838, https://doi.org/10.1002/we.1792.

——, and ——, 2017: A numerical study of wind-turbine wakes for three atmospheric stability conditions. *Bound.-Layer Meteor.*, **165**, 87–112, https://doi.org/10.1007/s10546-017-0259-9.

Zhang, W., C. D. Markfort, and F. Porté-Agel, 2013: Experimental study of the impact of large-scale wind farms on land-atmosphere exchanges. *Environ. Res. Lett.*, **8**, 015002, https://doi.org/10.1088/1748-9326/8/1/015002.

Zhou, L., Y. Tian, S. Baidya Roy, C. Thorncroft, L. F. Bosart, and Y. Hu, 2012: Impacts of wind farms on land surface temperature. *Nat. Climate Change*, **2**, 539–543, https://doi.org/10.1038/nclimate1505.

——, ——, ——, Y. Dai, and H. Chen, 2013: Diurnal and seasonal variations of wind farm impacts on land surface temperature over western Texas. *Climate Dyn.*, **41**, 307–326, https://doi.org/10.1007/s00382-012-1485-y.